Monthly Notices of the ROYAL ASTRONOMICAL SOCIETY

MNRAS **517,** 2028–2055 (2022) https://doi.org/10.1093/mnras/stac2598
Advance Access publication 2022 September 15

The effects of surface fossil magnetic fields on massive star evolution: IV. Grids of models at Solar, LMC, and SMC metallicities

Z. Keszthelyi [1,2★] A. de Koter,[1,3] Y. Götberg,[4†] G. Meynet,[5] S. A. Brands,[1] V. Petit [6] M. Carrington,[7] A. David-Uraz [8,9] S. T. Geen [1] C. Georgy,[5] R. Hirschi,[10,11] J. Puls,[12] K. J. Ramalatswa,[13,14] M. E. Shultz[6] and A. ud-Doula[15]

[1]*Anton Pannekoek Institute for Astronomy, University of Amsterdam, Science Park 904, NL-1098 XH Amsterdam, the Netherlands*
[2]*Center for Computational Astrophysics, Division of Science, National Astronomical Observatory of Japan, 2-21-1, Osawa, Mitaka, Tokyo 181-8588, Japan*
[3]*Institute of Astronomy, KU Leuven, Celestijnenlaan 200D, B-3001 Leuven, Belgium*
[4]*The Observatories of the Carnegie Institution for Science, 813 Santa Barbara Street, Pasadena, CA 91101, USA*
[5]*Geneva Observatory, University of Geneva, Maillettes 51, CH-1290 Sauverny, Switzerland*
[6]*Department of Physics and Astronomy, Bartol Research Institute, University of Delaware, 217 Sharp Lab, Newark, DE 19716, USA*
[7]*Department of Physics and Space Science, Royal Military College of Canada, PO Box 1700, Station Forces, Kingston, ON K7K 0C6, Canada*
[8]*Department of Physics and Astronomy, Howard University, Washington, DC 20059, USA*
[9]*Center for Research and Exploration in Space Science and Technology, and X-ray Astrophysics Laboratory, NASA/GSFC, Greenbelt, MD 20771, USA*
[10]*Astrophysics Group, Keele University, Keele, Staffordshire ST5 5BG, UK*
[11]*Institute for Physics and Mathematics of the Universe (WPI), University of Tokyo, 5-1-5 Kashiwanoha, Kashiwa 277-8583, Japan*
[12]*LMU München, Universitätssternwarte, Scheinerstr. 1, D-81679 München, Germany*
[13]*Department of Astronomy, University of Cape Town, Private Bag X3, Rondebosch 7701, South Africa*
[14]*South African Astronomical Observatory, PO Box 9, Observatory, 7935, Cape Town, South Africa*
[15]*Department of Physics, Penn State Scranton, 120 Ridge View Drive, Dunmore, PA 18512, USA*

Accepted 2022 September 9. Received 2022 August 25; in original form 2022 February 25

ABSTRACT

Magnetic fields can drastically change predictions of evolutionary models of massive stars via mass-loss quenching, magnetic braking, and efficient angular momentum transport, which we aim to quantify in this work. We use the MESA software instrument to compute an extensive main-sequence grid of stellar structure and evolution models, as well as isochrones, accounting for the effects attributed to a surface fossil magnetic field. The grid is densely populated in initial mass (3–60 $M_\odot$), surface equatorial magnetic field strength (0–50 kG), and metallicity (representative of the Solar neighbourhood and the Magellanic Clouds). We use two magnetic braking and two chemical mixing schemes and compare the model predictions for slowly rotating, nitrogen-enriched ('Group 2') stars with observations in the Large Magellanic Cloud. We quantify a range of initial field strengths that allow for producing Group 2 stars and find that typical values (up to a few kG) lead to solutions. Between the subgrids, we find notable departures in surface abundances and evolutionary paths. In our magnetic models, chemical mixing is always less efficient compared to non-magnetic models due to the rapid spin-down. We identify that quasi-chemically homogeneous main sequence evolution by efficient mixing could be prevented by fossil magnetic fields. We recommend comparing this grid of evolutionary models with spectropolarimetric and spectroscopic observations with the goals of (i) revisiting the derived stellar parameters of known magnetic stars, and (ii) observationally constraining the uncertain magnetic braking and chemical mixing schemes.

Key words: stars: abundances – stars: evolution – stars: magnetic field – stars: massive – stars: rotation.

1 INTRODUCTION

Magnetism is ubiquitously present in the Universe, from the scale of sub-atomic particles up to the scale of galaxy clusters (e.g. Neronov & Vovk 2010). For example, magnetic fields play a vital role in regulating star formation as molecular clouds collapse (e.g. Commerçon, Hennebelle & Henning 2011; Mackey & Lim 2011; Crutcher 2012; Hennebelle 2013; Körtgen & Soler 2020; Seifried et al. 2020), and in the formation and physics of neutron stars (e.g. Beloborodov 2009; Reisenegger 2009; Takiwaki, Kotake & Sato 2009; Takiwaki & Kotake 2011; Mösta et al. 2015; Kuroda et al. 2020; Aloy & Obergaulinger 2021; Reboul-Salze et al. 2021; Masada, Takiwaki & Kotake 2022). In the phase between star formation and stellar end products, massive star evolution remains uncertain in part due to the incomplete understanding of stellar magnetic fields.

Spectropolarimetric surveys revealed that a subset (about 10 per cent) of hot ($\gtrsim$ 10 kK), massive (8–60 $M_\odot$), and intermediate-mass (2–8 $M_\odot$) stars in the Galaxy with spectral types O, B, and A host large-scale, globally organised surface magnetic fields (Morel et al. 2015; Alecian et al. 2016; Fossati et al. 2016; Wade et al.

★ E-mail: zsolt.keszthelyi@nao.ac.jp
† Hubble Fellow

2016; Grunhut et al. 2017; Shultz et al. 2018; Petit et al. 2019; Sikora et al. 2019a). Surface magnetic fields are detected both in chemically peculiar Bp/Ap stars, as well as in O, B, and A stars without observed chemical peculiarities (e.g. Donati & Landstreet 2009; Henrichs et al. 2013; Neiner et al. 2015; Grunhut et al. 2017; Shultz et al. 2018; Sikora et al. 2019a). In addition, all known Of?p stars (showing variable emission in the CIII λ4647-4650-4652 complex, of comparable strength at its maximum to emission in the NIII λ4634-4640-4642 complex; Walborn 1972) in the Galaxy are observed to be magnetic.[1] Alongside spectropolarimetric observations, several properties may be used to identify magnetic candidates from photometric and spectroscopic studies, including multiwavelength diagnostics (e.g. Babel & Montmerle 1997; Cohen et al. 2003; Marcolino et al. 2012; Rivinius et al. 2013; Nazé et al. 2014; Oksala et al. 2015; Walborn et al. 2015; Buysschaert et al. 2018; Leto et al. 2021). Most recently, *TESS* photometric data is being used to identify candidate magnetic stars based on characteristic light-curve variations and subsequently observe them via spectropolarimetry (David-Uraz et al. 2019, 2021b; Sikora et al. 2019b; Shultz et al. 2019c, 2021a).

The observed surface magnetic fields of hot, massive, and intermediate-mass stars do not show any apparent correlation with stellar and rotational parameters unlike in lower mass ($<2\,M_{\odot}$), cool stars (<10 kK), where magnetism due to surface convection and differential rotation ubiquitously produce dynamo activity (Donati & Landstreet 2009; Neiner et al. 2015). Consequently, the organised, large-scale magnetic fields of hot stars are expected to be of fossil origin (Cowling 1945; Spitzer 1958; Mestel 1967, 2003; Moss 2003; Braithwaite & Spruit 2004, 2017; Mestel & Moss 2010; Ferrario, Melatos & Zrake 2015). The exact origin of observed magnetic fields remains debated. In about 10 per cent of intermediate-mass Herbig Be/Ae stars (which 10 per cent is thought to be the precursors of main sequence Bp/Ap stars), large-scale surface magnetic fields are already observed on the pre-main sequence (Stępień 2000; Alecian, Wade & Catala 2009; Alecian et al. 2013; Villebrun et al. 2019; Lavail et al. 2020), which may be acquired from the star-forming disc or generated via a dynamo action inside the star during a fully convective pre-main sequence phase (e.g. Moss 2003; Braithwaite 2012). In addition to magnetic fields possibly remaining from the star formation or pre-main sequence phases, stellar mergers could also amplify seed magnetic fields to a strength sufficient to be detectable (Ferrario et al. 2009; Wickramasinghe, Tout & Ferrario 2014; Schneider et al. 2016, 2019, 2020), suggesting that there may exist multiple channels to generate globally organised, large-scale fossil magnetic fields. Merger events of compact remnants have also been proposed to explain strongly magnetised white dwarfs and neutron stars (e.g. Tout et al. 2008; Giacomazzo et al. 2015; Ferrario, Wickramasinghe & Kawka 2020; Caiazzo et al. 2021; Shultz et al. 2021b).

The nature of fossil fields is fundamentally different from contemporaneously generated dynamo fields by a mechanical source (such as convection or differential rotation). Fossil field evolution is purely dissipative with no active field generation counteracting its slow dissipation (Braithwaite & Spruit 2017). In stellar layers where large-scale fossil fields spread through, it is expected that solid-body rotation will develop (e.g. Mestel 1999). In those stellar layers[2] the mechanical source of differential rotation is absent, and consequently small-scale dynamo fields in radiative stellar layers cannot be induced (Spruit 2004). The Tayler instability (Tayler 1973; Goldstein, Townsend & Zweibel 2019), for example, cannot develop if the radial rotation profile is completely flat, which means that the Tayler–Spruit (or 'Ω-type') dynamo cannot be induced in the presence of a fossil field (e.g. Spruit 2004). In fact, while this type of dynamo mechanism in radiative stellar layers was proposed by Spruit (2002), there remains ongoing debate about the necessary electromotive force to operate the dynamo cycle (Fuller, Piro & Jermyn 2019). The simulations of Zahn, Brun & Mathis (2007) suggest that this dynamo cycle does not operate. Despite the contradictory numerical results and the lack of direct observational evidence, dynamos in radiative stellar layers are commonly accounted for in evolutionary models (e.g. Spruit 2002; Maeder & Meynet 2003, 2004, 2005; Heger, Woosley & Spruit 2005; Yoon, Langer & Norman 2006; Denissenkov & Pinsonneault 2007; Maeder 2009; Potter, Chitre & Tout 2012b; Quentin & Tout 2018; Fuller et al. 2019; Fuller & Ma 2019; Takahashi & Langer 2021). We emphasise that these implementations are not suitable (at least directly) to model stars that are known to host fossil fields.

The time evolution of fossil magnetic fields also remains an unresolved problem. Observed samples of magnetic A-type stars and compact remnants are consistent with the magnetic flux being conserved over time (e.g. Wickramasinghe & Ferrario 2005; Landstreet et al. 2007, 2008; Neiner et al. 2017; Martin et al. 2018; Sikora et al. 2019a), whereas other observational evidence (including that for OB stars) suggests magnetic flux decay (e.g. Fossati et al. 2016; Shultz et al. 2019b). Fossil magnetic fields are expected to evolve only by Ohmic dissipation (Wright 1969; Spruit 2004; Duez & Mathis 2010; Braithwaite & Spruit 2017), which has a longer time-scale than the main sequence nuclear time-scale is (Cowling 1945; Spitzer 1958). However, Ohmic dissipation remains riddled with uncertainties depending on the exact value of magnetic diffusivity (e.g. Charbonneau & MacGregor 2001) and the geometry of the magnetic field since more complex fields dissipate faster.

Despite the uncertainties regarding the origin and evolution of fossil magnetic fields, it is now well established that they lead to various changes in stellar structure and evolution (e.g. Mestel 1989, 1999; Duez & Mathis 2010; MacDonald & Petit 2019; Jermyn & Cantiello 2020). Two main surface effects, mass-loss quenching and magnetic braking (discussed in detail below), have been shown to drastically modify evolutionary model predictions (e.g. Meynet, Eggenberger & Maeder 2011; Keszthelyi, Wade & Petit 2017a; Keszthelyi et al. 2019, 2020, 2021). For instance, heavy stellar-mass black holes and pair-instability supernovae could be formed from magnetic progenitors even at solar metallicity (Georgy et al. 2017; Petit et al. 2017)

Thus far, surface magnetic fields have only been detected in Galactic stars. Currently, high-resolution spectropolarimeters used for stellar magnetometry are employed on 4m-class telescopes, which limits observations to bright nearby stars. Using low-resolution spectropolarimetry, Bagnulo et al. (2017, 2020) searched for strong magnetic fields in the Magellanic Clouds through the Zeeman effect, which did not lead to definite detections in any of the targets. While high-resolution spectropolarimetry remains largely limited to a Galactic environment, very extensive spectroscopic campaigns in the Magellanic Clouds – in addition to the identified Of?p stars (e.g. Walborn et al. 2015; Munoz et al. 2020) – suggest that the nature of some stars may be explained by invoking surface magnetic fields (Hunter et al. 2008; Brott et al. 2011a; Potter et al. 2012b; Rivero González et al. 2012; Grin et al. 2017; Dufton et al. 2018, 2020; Ramachandran, Oskinova & Hamann 2021). Observations of known magnetic stars in the Galaxy are often compared to

[1]However, not all magnetic O-type stars belong to this class (Donati et al. 2002; Petit et al. 2013, 2017; Grunhut et al. 2017).

[2]However, dynamo-generated fields and fossil fields may co-exist in some stellar layers, for example, at the core-envelope interface (Featherstone et al. 2009). Whether such an interaction could lead to a more rapid dissipation of the fossil field remains an open question.

evolutionary models that do not include fossil field effects (e.g. those of Brott et al. 2011a; Ekström et al. 2012; Chieffi & Limongi 2013; Choi et al. 2016; Costa et al. 2021; Grasha et al. 2021), possibly making inferences of stellar parameters rather uncertain. In turn, this can largely impact the derived ages of individual stars and bias isochrone fitting of stellar clusters. Therefore, there is a need for stellar evolution models (and model grids), which take into account mass-loss quenching and magnetic braking (although see Potter et al. 2012b for the latter), thereby affecting detailed evolutionary model predictions and population synthesis studies in both Galactic and extragalactic environments.

The motivation of this study is to help to resolve these issues by presenting and studying an extensive grid of stellar structure and evolution models with metallicities typical of environments in the Solar neighbourhood,[3] Large Magellanic Cloud (LMC), and Small Magellanic Cloud (SMC) that include the effects of surface fossil magnetic fields. The model computations are open source and the entire library of models is available to the community via Zenodo at https://doi.org/10.5281/zenodo.7069766.

This paper is part of a series in which we aim to explore the effects of surface fossil magnetic fields on massive star evolution. In the first paper of the series (Keszthelyi et al. 2019, hereafter Paper I), we used the Geneva stellar evolution code (Eggenberger et al. 2008; Ekström et al. 2012; Georgy et al. 2013; Groh et al. 2019; Murphy et al. 2021) and discussed the mutual impact of magnetic mass-loss quenching, magnetic braking, and field evolution on a typical massive star of initially 15 $M_\odot$ at solar metallicity. We studied both solid-body and differentially rotating models and evaluated their key evolutionary characteristics, showing that strong surface nitrogen enrichment is expected for magnetic models with differential rotation. In the second paper (Keszthelyi et al. 2020, hereafter Paper II), we elaborated on the implementation of massive star magnetic braking in the MESA software instrument (Paxton et al. 2011, 2013, 2015, 2018, 2019) and detailed the magnetic and rotational evolution of the models by performing a parameter test in initial mass, magnetic field strength, and rotational velocity space with 35 models. Then, 72 tailored models were compared with a sample of observed magnetic B-type stars from Shultz et al. (2018, 2019a, b). A key finding of Paper II is that magnetic stars could originate from ZAMS progenitors with a variety of parameter combinations. In Paper III (Keszthelyi et al. 2021) we focused on the scenario that some magnetic stars may originate from rapidly rotating progenitors at the ZAMS, and specifically applied it to the case of the magnetic early B-type star τ Sco. We found that for this star the simultaneous nitrogen enrichment and slow rotation poses a significant challenge for single-star evolution.

The paper is organised as follows. In Section 2, we detail the assumptions and input physics used in the models. In Section 3, we present and scrutinise the stellar structure and evolution models from our computations. In Section 4, we discuss implications and future work. Finally, we conclude our findings in Section 5.

2 MODELLING ASSUMPTIONS AND SETUP

2.1 General strategy

In this work, we follow the general strategy of adopting suitable parametric prescriptions to model the effects of fossil magnetic fields, similar to the approaches presented in Paper I, Paper II, Paper III and references therein. While 1D magnetohydrodynamic (MHD) approaches are possible, they have mostly been developed for dynamo models (e.g. Feiden & Chaboyer 2012, 2013; Potter et al. 2012b; Quentin & Tout 2018; Takahashi & Langer 2021) and as such are not directly applicable to model fossil fields of intermediate-mass and massive stars. In particular, magnetic transport equations have been developed and used previously in the context of dynamo-generated fields (e.g. Spruit 2002; Maeder & Meynet 2003, 2004, 2005; Heger et al. 2005; Yoon et al. 2006; Potter et al. 2012b; Kissin & Thompson 2018; Quentin & Tout 2018; Fuller et al. 2019; Fuller & Ma 2019; Takahashi & Langer 2021). Although the characteristics (for example, the scale and time evolution) of dynamo models are incompatible with those of fossil fields (see Section 1), the transport equations may follow similar implementations. Here, we opt to artificially increase the diffusivity instead of testing 'magnetic' transport equations (Section 2.6.2). Such equations would introduce more free parameters and further assumptions regarding the geometry, structure, and radial dependence of the magnetic field. Clearly, further research and observational verification is required before an appropriate 1D magnetic transport process could be reliably incorporated to model stellar evolution with fossil magnetic fields (however, see Duez & Mathis 2010; Schneider et al. 2020). Duez & Mathis (2010) and Duez, Mathis & Turck-Chièze (2010) presented a comprehensive approach applicable for fossil fields, showing however that the impact on hydrodynamic equilibrium and energy transport are modest even for strong magnetic fields. To this extent, it is indeed appropriate to use parametric prescriptions and focus on the major, measurable effects[4] that fossil magnetic fields have, namely changing the mass loss (Section 2.5) and rotation (Section 2.6) of the star, affecting chemical mixing and angular momentum transport.

One of the major modelling challenges is that the geometry and alignment of the magnetic field play a significant role in the corresponding physical description. It has been demonstrated that a seed magnetic field can relax into a stable axisymmetric (around the magnetic axis) configuration if the magnetic flux is centrally concentrated, or into a non-axisymmetric (around the magnetic axis) configuration otherwise (Braithwaite & Spruit 2004; Braithwaite & Nordlund 2006; Braithwaite 2008). In both cases, the latitudinal averaging is inappropriate to model the magnetic field in 1D.[5]

For simplicity, we assume that the field is aligned with the rotation axis of the star since appropriate scaling relations for oblique fields (tilted with respect to the rotation axis) are still in development. However, the obliquity angles inferred from observations appear to follow a random distribution, which suggests that, apart from a few possible exceptions, massive stars generally possess magnetic fields that are inclined with respect to the rotation axis (e.g. Khalack, Zverko & Žižňovský 2003; Shultz et al. 2019a; Sikora et al. 2019a). Recent work from ud-Doula (2020) suggests that oblique rotation leads to decreasing the efficiency of magnetic braking. This effect could be incorporated in our models via a suitable scaling factor

[3] Since we follow the elemental abundance determinations given by Przybilla, Nieva & Butler (2008), Przybilla et al. (2013), Nieva & Przybilla (2012), and Asplund et al. (2009), we refer to this set of models as Solar and not Galactic.

[4] See e.g. Driessen, Sundqvist & Wade (2019a) for mass-loss quenching, and e.g. Townsend et al. (2010), Oksala et al. (2012), Song et al. (2022) for magnetic braking.

[5] For example, in the case of an axisymmetric dipole geometry, both poloidal and toroidal components must exist in the stellar interior (Braithwaite & Spruit 2004). The poloidal field strength and orientation relative to the normal to the surface varies over latitudes. The toroidal field, confined by closed poloidal lines, has zero strength along the polar rotation axis and reaches its maximum along the equatorial plane (see e.g. fig. 4 of Braithwaite 2008). A latitudinal averaging instead assigns a mean value to the poloidal and toroidal field components along a radius.

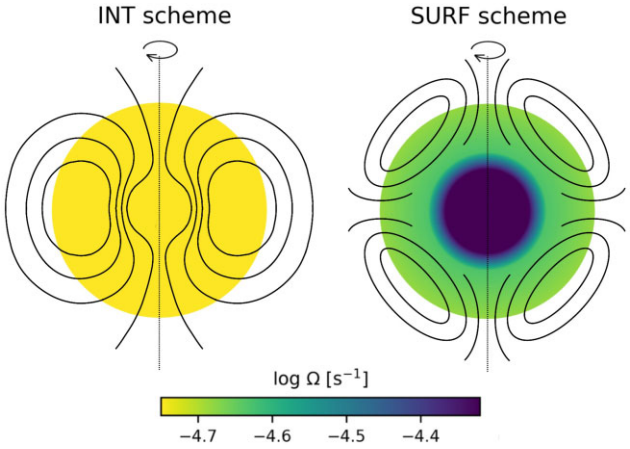

Figure 1. Schematic illustration of the magnetic field geometries (solid lines) considered in this study. These geometries are not directly implemented in our 1D models, instead they are used to constrain the corresponding scaling relations. Colours indicate the logarithmic angular velocity; the rotation axis is shown with dotted lines. Left-hand panel: INT scheme, representative of a dipolar field configuration leading to internal magnetic braking, spinning down all layers of the star. As a phenomenological picture, we assume that convective expulsion (see Appendix C (Supplementary)) would not allow the field to relax in the stellar core; however, we assume that the braking can propagate uniformly (including the core). The angular rotation is uniform throughout the star, enforced by a high diffusivity attributed to the dipole field. Right-hand panel: SURF scheme, representative of a more complex field geometry leading to surface magnetic braking. The magnetic energy can be stored in higher-order spherical harmonics, and twisted field lines only penetrate to some extent of the envelope which we assume to be 20 per cent of the mass fraction. In those layers efficient angular momentum transport is present but we assume that core-envelope coupling is not achieved. Magnetic braking is only applied to those upper layers (see Section 2.6.1). To be able to incorporate the effects of such fields into 1D models, we assume that a quadrupole scaling may be used for calculating the Alfvén radius.

in future studies. However, the efficiency of magnetic braking, in the evolutionary context, is also largely dependent on magnetic field evolution, which still needs to be better constrained (e.g. Paper III).

In fact, magnetic field evolution is closely tied to the question of the field geometry and, in this regard, new insights are gained from extensive monitoring campaigns, which can reveal the surface properties of magnetic fields. Although a purely dipolar field geometry generally matches observations (Grunhut et al. 2017; Shultz et al. 2018), modest deviations from pure dipolar geometries are now identified (Leto et al. 2018; Das, Chandra & Wade 2020; David-Uraz et al. 2021a). In other cases, contributions from higher-order harmonics are also identified (e.g. Shultz et al. 2018; Kochukhov, Shultz & Neiner 2019); however, the dipole is the strongest component, which consequently drives the main physical effects. In a few cases, observations have also identified stars with uniquely complex magnetic fields, which cannot be described with a dominant dipole component (e.g. τ Sco, Donati et al. 2006; Kochukhov & Wade 2016; Shultz et al. 2018). In these cases, most of the magnetic energy is stored in higher-order spherical harmonics, although a weak dipole contribution may still be present.

Since the structure of large-scale magnetic fields in stellar interiors is still considerably uncertain, we aim to test two limiting cases – illustrated in Fig. 1 – to apply depth-dependent magnetic braking (c.f. Paper II). In the models with internal magnetic braking (INT, described in detail below), we assume that the magnetic field is dipolar. We further assume that the field is present in the entire stellar envelope and is able to achieve core-envelope coupling (however, only as a phenomenological picture, we assume that it is excluded from the stellar core). In nature, the stellar envelope must also have a closed toroidal field for a stable configuration (Wright 1969, 1973; Braithwaite & Spruit 2004; Braithwaite & Nordlund 2006; Akgün et al. 2013), which we cannot directly take into account in our 1D models. The magnetic field is curl-free above the stellar surface; any toroidal field diffuses to a poloidal structure. We also introduce a set of models with surface magnetic braking (SURF, see also below) as a limiting scenario to contrast the INT models with. The complex magnetic field geometries clearly cannot be translated to our 1D models, therefore we make various simplifying assumptions (discussed in detail throughout Section 2). We reiterate that the field geometry cannot be directly included in our models, only via the scaling relations. The limitations related to the 1D parametrisation can likely only be resolved once 2D stellar evolution modelling becomes feasible (Espinosa Lara & Rieutord 2011; Lovekin 2020; Reese et al. 2021).

Angular momentum is always lost from the outermost layers of the star. We use the INT/SURF schemes to control the propagation of this loss to the stellar interiors along with efficient angular momentum transport. In the INT models, all stellar layers efficiently transport and lose specific angular momentum. Motivated by the simulations of Braithwaite (2008), we assume that in the SURF models the magnetic-field driven angular momentum transport and rotational braking only affect the upper 20 per cent of stellar mass. Although even for complex surface magnetic fields there may be weak dipole contributions, we neglect here any possible magnetic angular momentum transport in the deep stellar interiors so that we are able to test a limiting case in which radial differential rotation may develop in regions of the star where the magnetic flux is assumed to be negligible. Furthermore, to generalise from the range of possible field configurations deduced from observations, we assume that at least the Alfvén radius (see section 2.4) has to be smaller in the SURF models than in the INT models for a given surface field strength. For this reason, we use a quadrupole scaling in the SURF models to obtain the Alfvén radius. This results in less efficient magnetic braking for complex fields compared to dipole-dominated geometries. The field geometry defines the wind flow and mass flux from the stellar surface. We evaluate in Appendix B (Supplementary) how an actual quadrupole field geometry would affect mass-loss quenching; however, since this effect only concerns the highest-mass models, for simplicity we adopt a formalism where only the Alfvén radius is changed in the SURF models compared to the INT models (see Section 2.5).

2.2 General model setup

We use the software instrument Modules for Experiments in Stellar Astrophysics MESA release 15140 (Paxton et al. 2011, 2013, 2015, 2018, 2019) and Software Development Kit (SDK) version 20.12.1 (Townsend 2020), and carry out our computations on the Dutch supercomputers Cartesius[6] and Snellius.[7] In this study, we consider main sequence models with initial masses from 3 to 60 $M_\odot$ (Table 1). This choice is made since there are still considerable uncertainties in stellar evolution, as well as in magnetic field evolution on the post-main sequence. The computations begin by relaxing the initial model and we consider the Zero Age Main Sequence (ZAMS) to begin at the time when the initial abundance of core hydrogen has decreased by 0.3 per cent. The endpoint of the models is the Terminal Age Main Sequence (TAMS), which we consider at the time when the core hydrogen mass fraction drops below 10^{-5}.

[6]https://userinfo.surfsara.nl/systems/cartesius
[7]https://userinfo.surfsara.nl/systems/snellius

Table 1. Comprehensive grid of 8,748 MESA evolutionary models including the effects of surface fossil magnetic fields, covering a large parameter space in initial mass and magnetic field strength (see below) for 3 metallicities (Table 2) and for 2 braking schemes and 2 mixing schemes (Table 3).

$M_{\star,\,\mathrm{ini}}$ [$M_\odot$]	3, 4, 5, 6, 7, 8, 9, 10, 11, 12, 13, 14, 15, 16, 17, 18, 19, 20, 21, 22, 23, 24, 25, 30, 40, 50, 60
$B_{\mathrm{eq,\,ini}}$ [kG]	0, 0.25, 0.50, 0.75, 1.0, 1.5, 2.0, 2.5, 3.0, 3.5, 4.0, 4.5, 5.0, 5.5, 6.0, 6.5, 7.0, 7.5, 8.0, 8.5, 9.0, 9.5, 10, 15, 20, 30, 50

The MESA microphysics are summarized in Appendix A (Supplementary). To calculate the nuclear reaction rates, we use MESA's default 'basic.net' option. To model convective mixing, we assume a mixing length parameter of $\alpha_{\mathrm{MLT}} = 1.8$ (e.g. Canuto & Mazzitelli 1992; Canuto, Goldman & Mazzitelli 1996) and the Henyey formalism (Henyey, Vardya & Bodenheimer 1965) in MESA. Common values of α_{MLT} range from 1.5 to 2.0, mostly based on solar and solar-type star calibrations (e.g. Bonaca et al. 2012). For simplicity, we assume the same value in all models, although some studies predict mass dependence (e.g. Yıldız et al. 2006). Semiconvective and thermohaline mixing are not used.[8] Convective boundaries are determined via the Ledoux criterion. Core overshooting is applied in the exponential scheme with parameters $f_{\mathrm{ov}} = 0.015$ and $f_0 = 0.005$, which roughly corresponds to a step overshoot parameter α_{ov} of 10 per cent of the local pressure scale height (Ekström et al. 2012, see further discussion in Appendix C (Supplementary)). α_{ov} may be mass dependent (Castro et al. 2014). Commonly used values of α_{ov} range from 0.1 to 0.335, (Schaller et al. 1992; Brott et al. 2011a). Exponential overshooting at non-burning convective regions is adopted with $f_{\mathrm{ov}} = 0.0010$ and $f_0 = 0.0005$. MESA's MLT++ scheme is not applied (see e.g. Poniatowski et al. 2021).

We employ high spatial and temporal resolution by setting `mesh_delta_coeff = 1.` and `time_delta_coeff = 1.`, in addition to setting `varcontrol_target = 1.d-4`. This results in an average of 2000–3000 zones for our stellar structure models, and the evolutionary models consist of a hundred to a few thousand structure models (each corresponding to one time step), mostly depending on the initial mass.

We consider one initial rotation rate[9] in all models by relaxing an initial ratio of $\Omega/\Omega_{\mathrm{crit}} = 0.5$. In our models with solar metallicity, this approximately corresponds to an initial equatorial surface rotational velocity (`surf_avg_vrot` in MESA) of 300 to 370 km s^{-1} in the initial stellar mass range from 3 to 60 $M_\odot$. The critical angular velocity is adopted as defined in MESA `star_utils.f90`:

$$\Omega_{\mathrm{crit}} = \sqrt{(1-\Gamma)\frac{Gm}{r^3}}\,, \tag{1}$$

where the Eddington parameter is $\Gamma = L_{\mathrm{rad}}/L_{\mathrm{Edd}}$, G is the gravitational constant, and m and r are the mass and radius taken at the photosphere. This definition only plays a role in setting the initial rotational velocity.[10] The initial model relaxes from solid-body rotation to a new configuration constrained by angular momentum distribution and transport.

In Paper II, we found that a lower rotation rate (initially $\Omega/\Omega_{\mathrm{crit}} = 0.2$) leads to smaller differences between models with and without magnetic fields. This is simply because magnetic braking is less efficient when the rotation is slow.[11] In Paper II, we showed that at least a few magnetic stars were best matched with models that had an initial rotation rate of $\Omega/\Omega_{\mathrm{crit}} = 0.8$. If the initial rotation rate was higher than considered in this study, it would (i) alter the early evolution of the models on the Hertzsprung–Russell diagram (HRD, as shown in fig. 3 of Paper II), and (ii) impact the quantitative predictions regarding the surface chemical enrichment. It is worth noting that the most rapidly rotating (presumably young) magnetic stars have present-day surface rotational velocities of about 300 km s^{-1}, which is close to 50 per cent of the critical rotation defined in our equation (1) (e.g. Oksala et al. 2010; Grunhut et al. 2012; Shultz et al. 2019b; Song et al. 2022). Nevertheless it remains unknown what initial rotation rates could characterise the entire sample of magnetic massive stars.

Finally, given the supporting observational evidence by some studies (Wickramasinghe & Ferrario 2005; Kochukhov & Bagnulo 2006; Neiner et al. 2017; Martin et al. 2018; Sikora et al. 2019a), we assume magnetic flux conservation (Alfvén's theorem, Alfvén 1942) such that the surface magnetic field strength is obtained from:

$$B_{\mathrm{eq}} = B_{\mathrm{eq,\,ini}}\left(\frac{R_{\star,\mathrm{ini}}}{R_\star}\right)^2 \tag{2}$$

with $B_{\mathrm{eq,\,ini}}$ being the initial surface equatorial magnetic field strength (which is assumed in the models at the ZAMS), while $R_{\star,\,\mathrm{ini}}$ and $R_\star$ are the initial and current stellar radii. For further discussions on magnetic field evolution, we refer the reader to Paper I, Paper II, Paper III, and references therein. We adopt a large range of initial equatorial magnetic field strengths (from 0 to 50 kG; e.g. Donati & Landstreet 2009; Shultz et al. 2019b.)

The `run_star_extras` file (available as part of a full reproduction package on Zenodo) is used to modify the wind, torque, angular

[8]Neither of these mixing mechanisms is expected to significantly change main sequence models. It was shown by Charbonnel & Zahn (2007) that a strong magnetic field could inhibit thermohaline mixing in descendants of Ap stars (see also e.g. Denissenkov, Pinsonneault & MacGregor 2009). On the other hand, Harrington & Garaud (2019) finds that thermohaline mixing could be enhanced by an aligned magnetic field.

[9]The actual initial rotation rate of stars in general remains an open question. Spectroscopic studies have focused on large samples to obtain the distribution of projected rotational velocities in the Galaxy (Howarth et al. 1997; Huang, Gies & McSwain 2010; Simón-Díaz & Herrero 2014; Simon-Diaz et al. 2016; Simón-Díaz et al. 2017, Holgado et al. 2022) and in the Magellanic Clouds (Martayan et al. 2006, 2007; Ramírez-Agudelo et al. 2013, 2015; Dufton et al. 2019, 2020). The findings indicate a Gaussian distribution of $v\sin i$, with different peak values depending on physical (spectral type, mass, etc.) and observational characteristics (sample size, magnitude limit, etc.). The typical peaks of the distributions are around 100 km s^{-1}. Considering that this value needs to be corrected for the (usually unknown) inclination angles and that it reflects on the current rotation after a given star or population have evolved away from the ZAMS, it is generally assumed that the canonical initial rotational velocities of massive stars are of the order of 300 km s^{-1}. Although for Galactic O-stars the IACOB survey (Simón-Díaz & Herrero 2014; Simon-Diaz et al. 2016; Simón-Díaz et al. 2017, Holgado et al. 2022) has shown somewhat lower values than previous studies ($\approx$ 100–200 km s^{-1}), which could be consistent with lower initial rotational velocities. Our chosen input parameter for the initial rotation rate of $\Omega/\Omega_{\mathrm{crit}} = 0.5$ reflects closely on the canonical value around 300 km s^{-1}, identified in the sample of Howarth et al. (1997).

[10]In fact, in MESA the Eddington luminosity is calculated from the total opacity. Since the precise definition of Ω_{crit} is significantly more complex (see Puls, Vink & Najarro 2008 for further discussion), we stress here that Ω_{crit} is only used as an input option to set the rotational velocity.

[11]In Paper I, we also demonstrated that for a typical non-rotating 15 $M_\odot$ model at solar metallicity, mass-loss quenching is modest. As shown by Petit et al. (2017), who computed non-rotating solar metallicity models between 40 and 80 $M_\odot$, the evolutionary impact of magnetic mass-loss quenching becomes significant at higher masses.

Table 2. Key initial elemental abundances (in mass fractions and compared to the adopted solar value) included in our models.

	X_{ini}	$\frac{X_{ini}}{X_{\odot,ini}}$	Y_{ini}	$\frac{Y_{ini}}{Y_{\odot,ini}}$	Z_{ini}	$\frac{Z_{ini}}{Z_{\odot,ini}}$	C_{ini}	$\frac{C_{ini}}{C_{\odot,ini}}$	N_{ini}	$\frac{N_{ini}}{N_{\odot,ini}}$	O_{ini}	$\frac{O_{ini}}{O_{\odot,ini}}$
Solar	0.72000	1	0.26600	1	1.40000×10^{-2}	1	1.84720×10^{-3}	1	6.21528×10^{-4}	1	6.62907×10^{-3}	1
LMC	0.73685	1.02	0.25671	0.97	6.43605×10^{-3}	0.46	9.25898×10^{-4}	0.50	1.45717×10^{-4}	0.24	2.96143×10^{-3}	0.45
SMC	0.74840	1.04	0.24900	0.94	2.60758×10^{-3}	0.19	2.15433×10^{-4}	0.12	6.76488×10^{-5}	0.11	1.34354×10^{-3}	0.20

Table 3. Magnetic braking and chemical mixing schemes.

INT:	Solid-body rotation, braking the rotation of the entire star
SURF:	Differential rotation, braking the rotation of the surface
Mix1:	D_{chem} defined by equation (16) with $f_c = 0.033, f_\mu = 0.1$
Mix2:	D_{chem} defined by equation (22) with $f_c = 1, f_\mu = 1$

momentum transport, and chemical element transport routines. The parameters varied in the models are summarized in Tables 1, 2, and 3, and are discussed below.

2.3 Metallicity

We compute models for three different metallicities (the key elements are summarized in Table 2 – the full list of abundances is available via the model files shared on Zenodo) that are representative of the Solar neighbourhood, LMC, and SMC. For the Solar composition, we assume the hydrogen and helium mass fractions along with a metallicity of $Z = 0.014$ (Asplund et al. 2009). The metal fractions are adopted following the works of Przybilla et al. (2008, 2013) and Nieva & Przybilla (2012), which updated some elements compared to the Asplund, Grevesse & Sauval (2005), Asplund et al. (2009) abundances, considering B-type stars in the solar neighbourhood. The baseline values for the Magellanic Clouds are still subject to ongoing investigations (e.g. Dufton et al. 2020; Bouret et al. 2021). For the helium and metal abundances in the LMC and SMC, we adopt the mean values listed in tables 5 and 6 of Dopita et al. (2019). These mean values are a result of nine separate investigations using different approaches, which include atmospheric determinations of hot stars, supernova remnants, and H II regions. In all three metallicities, we use the Lodders (2003) isotopic ratios. The metallicity adopted for the chemical composition is fully consistent with the metallicity used for the opacity tables.

2.4 Alfvén radius

The Alfvén radius characterises a critical distance at which the magnetic energy density and the gas kinetic energy density are equal. Alternatively, it can also be cast as the inverse square of the Alfvénic Mach number. Its definition plays an important role in both mass-loss quenching (equations 7–8) and magnetic braking (equations 9–10). For a dipolar field configuration, ud-Doula, Owocki & Townsend (2009) use a numerical fitting for a quartic equation to obtain:

$$\frac{R_A}{R_\star} \approx 1 + (\eta_\star + 0.25)^{1/4} - (0.25)^{1/4}\,, \tag{3}$$

with $\eta_\star$ the equatorial magnetic confinement parameter, defined as:

$$\eta_\star = \frac{B_{eq}^2 R_\star^2}{\dot{M}_{B=0} v_\infty}\,, \tag{4}$$

with B_{eq} the equatorial magnetic field strength, $\dot{M}_{B=0}$ the mass-loss rate in absence of a magnetic field, and v_∞ the terminal velocity[12] (ud-Doula et al. 2009). Observations typically reconstruct a polar field strength B_p from the line-of-sight disc-integrated (the so-called longitudinal) magnetic field strength (Donati & Landstreet 2009). The equatorial field strength is exactly one half of the polar field strength. We use equation (3) to obtain the Alfvén radius in the INT models, which we assume to be characterised by a predominantly dipolar field configuration (Fig. 1). In the SURF models we assume the field to be more complex, in which case the definition of the Alfvén radius is non-trivial. For the sake of simplicity we assume that the Alfvén radius takes the form of a scaling appropriate for a quadrupole field geometry, such that:

$$\frac{R_A}{R_\star} \approx 1 + (\eta_\star + 0.25)^{1/6} - (0.25)^{1/6}\,, \tag{5}$$

following the parametrization in equation (9) of ud-Doula, Owocki & Townsend (2008). This ensures that for a given field strength R_A is less in the SURF case than in the INT case, leading to less efficient magnetic braking.

2.5 Stellar winds

2.5.1 *Mass-loss schemes and terminal velocities*

The models include mass loss. Even though this is modest for the lower-mass stars (and the driving mechanism is not unambiguously identified as for more massive stars), it can impact their rotational evolution given the longer nuclear time-scale. For this reason, we apply commonly used mass-loss rates of hot massive stars also to lower mass main sequence stars in our grid. While the higher-mass stars typically reach the TAMS at $T_{eff} > 20$ kK, we describe here the detailed treatment implemented in our MESA extension for completeness and to aid further studies focusing on complementing this work with post-main sequence models. For massive stars with $T_{eff} > 10$ kK, the mass-loss is powered by radiative line driving (e.g. Lucy & Solomon 1970; Castor, Abbott & Klein 1975; Puls et al. 2008). In this regime, we apply the rates derived by Vink, de Koter & Lamers (2000), Vink, de Koter & Lamers (2001), decreased by a factor of 2 for all models in the 3–60 $M_\odot$ range for consistency. The choice to reduce the nominal mass-loss rates is motivated by the growing evidence both from observations, suggesting that mass-loss rates are lower when accounting for wind clumping L(e.g. Bouret, Lanz & Hillier 2005; Trundle & Lennon 2005; Fullerton, Massa & Prinja 2006; de Almeida et al. 2019; Brands et al. 2022), and from new modelling approaches (e.g. Muijres et al. 2012; Krtička 2014; Krtička & Kubát 2017; Sundqvist et al. 2019; Björklund et al. 2021; Krtička, Kubát & Krtičková 2021). When using these rates, we apply metallicity-dependent winds with a scaling of $\dot{M} \sim Z^{0.85}$ (e.g. Vink et al. 2001; Mokiem et al. 2007).

[12] Also calculated for in absence of a magnetic field.

Similarly to Keszthelyi, Puls & Wade (2017b) and Paper II, we implement the partitioning in effective temperature related to the bi-stability jump at 20 kK in agreement with observational and new theoretical works (Prinja, Barlow & Howarth 1990; Lamers, Snow & Lindholm 1995; Prinja & Massa 1998; Petrov, Vink & Gräfener 2016), rather than adopting it at 25–27 kK as in evolutionary models of e.g. Brott et al. (2011a), Ekström et al. (2012), and Choi et al. (2016). This is further supported by measurements of projected rotational velocities that suggest a lack of bi-stability braking (Crowther, Lennon & Walborn 2006; Vink et al. 2010; Keszthelyi et al. 2017b; Gagnier et al. 2019a, b; Krtička et al. 2021; Vink & Sander 2021) at least until about 20 kK (Howarth et al. 1997; Huang et al. 2010). Although we adopt an increase in mass-loss rates at the bi-stability jump, we note that this prediction still lacks empirical evidence in typical B-type supergiants (Crowther et al. 2006; Markova & Puls 2008; Rubio-Díez et al. 2022) and is challenged by new numerical simulations (Sundqvist et al. 2019; Driessen, Sundqvist & Kee 2019b; Björklund et al. 2021).

Below approximately 10 kK the nature of wind-driving remains poorly understood. We opt to use the rates of van Loon et al. (2005) for all models in this domain, which only concerns a few lower-mass models in the present grid. New modelling approaches have confirmed that the second bi-stability jump due to Fe III recombining to Fe II is expected at $T_{\rm eff} \sim 9$ kK (Petrov et al. 2016) in contrast with earlier indications of $\sim$ 12.5 kK (Vink, de Koter & Lamers 1999; Vink et al. 2000), and implementations in evolutionary models of $\sim$ 17–15 kK (Brott et al. 2011a; Ekström et al. 2012). Therefore we avoid the use of the second bi-stability jump that is typically included in other grids of models (for further details see, e.g. fig. 3 of Keszthelyi et al. 2017b). If the effective temperature is higher than 10 kK and the surface hydrogen mass fraction becomes less than 0.4, we apply the Wolf–Rayet rates of Nugis & Lamers (2002). This concerns some of our most massive models with efficient mixing.

In agreement with the partitionings in effective temperature, we estimate the terminal wind velocity v_∞ via:

$$v_\infty = f_\infty \cdot v_{\rm esc} = f_\infty \sqrt{\frac{2GM_\star}{R_\star}(1-\Gamma_e)}, \tag{6}$$

where G, $M_\star$, $R_\star$, and Γ_e are, respectively, the gravitational constant, the stellar mass, the stellar radius, and the Eddington parameter for pure electron scattering. The terminal wind velocity is obtained from the escape velocity as a simple step function by adopting $f_\infty = 2.6$, 1.3, 0.7 at $T_{\rm eff} > 20$ kK, 20 kK $> T_{\rm eff} > 10$ kK, and $T_{\rm eff} < 10$ kK, respectively (Lamers et al. 1995; Kudritzki & Puls 2000; Vink et al. 2000). The typical terminal velocities at the ZAMS range from 800 to 3000 km s^{-1} for models with initial masses from 3 to 60 $M_\odot$, respectively. We calculate the rotational enhancement on the mass-loss rates[13] as described by Maeder & Meynet (2000). This requires defining the difference of the force multiplier parameters α' ($=\alpha - \delta$, that is, the exponent related to the line-strength distribution function minus the exponent quantifying the change in ionisation balance), which we adopt as a simple step function with values of 0.6, 0.5, 0.4, corresponding to the above-mentioned effective temperature ranges (see Pauldrach, Puls & Kudritzki 1986; Lamers et al. 1995; Puls, Springmann & Lennon 2000). The alternative calculation of rotational enhancement built into MESA is not used (see Paper II Section 3.9 for details).

[13] See also the recent study of Brinkman et al. (2021).

2.5.2 *Magnetic mass-loss quenching*

The overall field configuration that extends into the wind outflow is governed by the competition between the kinetic energy of the wind and the magnetic energy of the field. The ionized stellar wind material is forced to flow along magnetic field lines. However, as the wind kinetic energy density has a shallower decline than the magnetic energy density, the field loops can only confine wind material up to a certain radius. Within closed field loops, material becomes trapped and eventually falls back on to the surface (unless centrifugally supported). To account for the global, time-averaged effect of the magnetosphere, the mass-loss rates are systematically reduced. Following the works of ud-Doula et al. (2008), ud-Doula et al. (2009), the mass-loss quenching parameter $f_{\rm B}$ is defined as:

$$f_{\rm B} = \frac{\dot{M}}{\dot{M}_{B=0}} = 1 - \sqrt{1 - \frac{1}{R_{\rm c}}} \quad \text{if} \quad R_{\rm A} < R_{\rm K} \tag{7}$$

and

$$f_{\rm B} = \frac{\dot{M}}{\dot{M}_{B=0}} = 2 - \sqrt{1 - \frac{1}{R_{\rm c}}} - \sqrt{1 - \frac{0.5}{R_{\rm K}}} \quad \text{if} \quad R_{\rm K} < R_{\rm A}, \tag{8}$$

where $R_{\rm A}$, $R_{\rm K}$, and $R_{\rm c}$ are the Alfvén radius, the Kepler co-rotation radius, and the closure radius in units of the stellar radius, respectively (see Petit et al. 2017, Paper I, Paper II, Paper III, and references therein). The closure radius, defining the distance from the stellar surface to the last closed magnetic loop, is approximated as $R_{\rm c} \sim R_\star + 0.7\ (R_{\rm A} - R_\star)$, see ud-Doula et al. (2008). $\dot{M}$ is the mass-loss rate that a non-rotating magnetic star would have. $\dot{M}$ is further scaled by the rotational enhancement $f_{\rm rot}$ (specified in Section 3.9 of Paper II) such that the effective mass-loss rate is obtained from $\dot{M}_{\rm eff} = f_{\rm B} \cdot f_{\rm rot} \cdot \dot{M}_{B=0}$. The magnetic mass-loss quenching parameter (equivalent to the escaping wind fraction[14]) can take values between 0 and 1, depending on the magnetic field strength. A strong magnetic field (with a strength of tens of kG) may lead to only a few per cent of the wind material actually escaping the star (Georgy et al. 2017; Petit et al. 2017; Paper I). Let us also note that the conditions in the above equations are equivalent to distinguishing between dynamical magnetospheres (if $R_{\rm A} < R_{\rm K}$) and centrifugal magnetospheres (if $R_{\rm K} < R_{\rm A}$), a classification introduced by Petit et al. (2013).

The use of equation (8) is a refinement compared to previous implementations. For situations when the Alfvén radius is larger than the Kepler co-rotation radius (centrifugal magnetospheres), the magnetosphere is expected to be less efficient at quenching wind mass-loss compared to dynamical magnetospheres (ud-Doula et al. 2008, 2009). This is because material injected by the wind into the centrifugal magnetosphere is not returned to the stellar surface by gravity, but is instead ejected away from the star once the critical centrifugal breakout density is exceeded (Owocki et al. 2020; Shultz et al. 2020). This can lead to substantially larger values of $f_{\rm B}$ for a rotating as compared to a non-rotating star, however in practice rapid spin-down means that centrifugal magnetospheres are relatively short-lived and the incorporation of this modification to the mass-quenching prescription does not have a strong effect on evolution. It is generally expected that the evolution proceeds from centrifugal to dynamical magnetospheres (Shultz et al. 2019b, Paper I, Paper II).

In this approach, the magnetic mass-loss quenching parameter is an average quantity. MHD simulations of non-rotating magnetospheres

[14] Calculated for different $R_{\rm A}$ in the INT and SURF schemes; however, see Appendix B (Supplementary) for an actual quadrupole geometry.

predict up- and down-flows of material varying on short dynamical time-scales (ud-Doula & Owocki 2002), which can manifest as stochastic variability in magnetospheric emission lines (ud-Doula et al. 2013), however time-averaged models provide a good reproduction of emission line properties (e.g. Sundqvist et al. 2012; Owocki et al. 2016; Erba et al. 2021) and these short-term, stochastic variations can therefore be confidently neglected over evolutionary time-scales. In the case of rapid rotators, 2D MHD simulations led to the expectation that breakout events would be similarly stochastic, leading to emptying of the centrifugal magnetosphere and large-scale magnetospheric reorganisation (ud-Doula, Townsend & Owocki 2006; ud-Doula et al. 2008). However, no indication of large-scale changes has been observed (Townsend et al. 2013; Shultz et al. 2020), leading Shultz et al. (2020) and Owocki et al. (2020) to infer that breakout events are characterised by small spatial scales and occur more or less continuously, such that the centrifugal magnetosphere is maintained nearly continuously at the breakout density. As a result, it is therefore appropriate to treat magnetospheric mass-drainage via breakout as an effectively continuous process over evolutionary time-scales and apply equations (7) and (8).

2.6 Angular momentum transport and loss

Magnetic fields are much more efficient at transporting angular momentum than purely hydrodynamic processes such as meridional currents and shear instabilities (e.g. Mestel 1999; Spruit 1999, 2002; Kulsrud 2005; Braithwaite & Spruit 2017). The rotation of the star leads to Maxwell stresses, which result in losing angular momentum from the star.

In Paper I, GENEC models were used, where magnetic braking is adopted as a boundary condition to internal angular momentum transport, directly affecting the uppermost layer of the stellar models. In Paper II, two kinds of models were introduced to account for the uncertainty regarding how deeply fossil magnetic fields are anchored in massive stars. In the INT models, magnetic braking was applied to the entire star, decreasing uniformly the specific angular momentum in all layers. In the SURF models, magnetic braking was set to remove specific angular momentum from a very near-surface reservoir. In Paper III, GENEC models were contrasted with a MESA implementation where magnetic braking was applied to most of the stellar envelope. In GENEC, two configurations were used to model internal angular momentum transport: one with only hydrodynamic instabilities correctly accounted for via an advecto-diffusive equation (allowing for shears to develop in deeper layers), and one with a purely diffusive equation, in which solid-body rotation was established. In MESA, we relied on the nominal hydrodynamic transport processes since they are used in a purely diffusive assumption, leading to nearly solid-body rotation on the magnetic braking time-scale. Here, we make some further refinements and adjustments compared to these approaches, particularly accounting (indirectly) for the field geometry as depicted in Fig. 1.

2.6.1 *Magnetic braking*

Stellar rotation bends and twists magnetic field lines in the azimuthal direction. Magnetic field lines can transport and store angular momentum, and the associated Maxwell stresses are very efficient at transferring angular momentum to the surrounding plasma. Once the angular momentum is imparted from the field to the gas, the wind material carries it away, leading to a spin-down of the star. This process is commonly referred to as (wind) magnetic braking.

In a pioneering series of works, analytical and numerical MHD simulations were developed, confirming that the Weber & Davis (1967) model (see also, Parker 1958; Mestel 1968) leads to an appropriate scaling relation also for massive stars (ud-Doula & Owocki 2002; Owocki & ud-Doula 2004; Townsend & Owocki 2005; ud-Doula et al. 2008, 2009). Following the work of ud-Doula et al. (2009), the total – wind and magnetic field induced – loss of angular momentum can be expressed via:

$$\frac{\mathrm{d}J_\mathrm{B}}{\mathrm{d}t} = \frac{2}{3}\dot{M}_{B=0}\,\Omega_\star R_A^2\,, \tag{9}$$

with $\mathrm{d}J_\mathrm{B}/\mathrm{d}t$ the rate of angular momentum loss from the system, $\Omega_\star$ the surface angular velocity, and R_A the Alfvén radius (defined in equations 3 and 5). As this equation accounts for the gas and field driven angular momentum loss (ud-Doula et al. 2009), it yields the angular momentum loss resulting purely from mass loss when $B_\mathrm{surf} = 0$. As specified in Paper II, we have adjusted the angular momentum lost via mass loss to avoid double counting. In equation (9), the numerical term 2/3 arises from integrating over latitudes. We note that this equation is not applicable when the effective mass-loss rate, as introduced above, is exactly zero (this situation does not happen in our models). In the strong confinement limit, when $f_\mathrm{B} \rightarrow 0$, the effective mass-loss rate can become very small. In this case, a strong magnetic braking can still be achieved since the Maxwell stresses driving the angular momentum transport are independent of the plasma flow. As long as there is wind material at a radial distance larger than the last closed magnetic field line, i.e. the star is not surrounded by vacuum, the field can impart angular momentum to the plasma. In Paper II and Paper III, equation (9) was implemented into MESA via changing the specific angular momentum in given layers of the star, such that a summation over mass yields the total rate of angular momentum loss as defined in equation (9). It is coded as:

$$\frac{\mathrm{d}J_\mathrm{B}}{\mathrm{d}t} = \sum_{k=1}^{k=x}\frac{\mathrm{d}j_\mathrm{B}}{\mathrm{d}t} = -\frac{\mathrm{d}J_\mathrm{B}}{J_\mathrm{INT/SURF}}\sum_{k=1}^{k=x}\frac{\mathrm{d}j}{\mathrm{d}t}\,, \tag{10}$$

where $\mathrm{d}j_\mathrm{B}/\mathrm{d}t$ is the rate of specific angular momentum change (dubbed as '`extra_jdot`' in MESA). The negative sign is added to reduce the reservoir (i.e. to account for loss), $\mathrm{d}J_\mathrm{B} = (\mathrm{d}J_\mathrm{B}/\mathrm{d}t)\cdot dt$ is the total angular momentum lost per time $\mathrm{d}t$, $J_\mathrm{INT/SURF}$ is the angular momentum reservoir of the entire star (INT) or of defined layers in the stellar envelope (SURF; see Fig. 1 and discussion below), j is the specific angular momentum of a layer (called '`j_rot`' in MESA), $\mathrm{d}t$ is one timestep in the computation,[15] k is an index running through all layers, and x is the index of the last layer where magnetic braking is applied. Therefore, equation (10) indicates how to distribute the total angular momentum lost per unit time ($\mathrm{d}J_\mathrm{B}/\mathrm{d}t$ given by equation 9) in given stellar layers. Taking the sum of the specific angular momentum lost per unit time $\mathrm{d}j_\mathrm{B}/\mathrm{d}t$ with respect to mass, we recover the left-hand side term.

To distribute the total angular momentum lost per unit time, the summation goes over the layers of the entire star in the INT case ($x \approx$ 3000 zones), whereas in the SURF case it goes from the photosphere to a lower boundary. This boundary is always in the radiative stellar envelope of our models. However, more massive models have larger convective cores, and thus for very massive stars (>60 $\mathrm{M}_\odot$), this condition may need to be revised as we do not expect the fossil field to be able to penetrate into the convective core. In the SURF models, x

[15] We use a time-step control, specified in Paper II, which prevents the star model from fully exhausting specific angular momentum in any layer.

≈ 200 zones undergo magnetic braking. Here, we chose the boundary layer where $q = m/M_\star = 0.8$ (the enclosed mass is 80 per cent of the total mass) since Braithwaite (2008) demonstrated that complex, non-axisymmetric fields (around the magnetic axis) can form if the magnetic flux is initially not centrally concentrated, leading to a stable magnetic field configuration in which twisted magnetic field lines spread throughout the stellar surface layers. In the simulations of Braithwaite (2008), a strong toroidal field (enclosed by poloidal field lines) is present in approximately 20 per cent of the upper mass fraction and this motivates our choice for this parameter.

2.6.2 *Angular momentum transport*

The main impact of the angular momentum transport equation in stellar interiors is to change the angular velocity profile $\Omega(r)$, which is also measurable via modern asteroseismology (see e.g. Aerts, Mathis & Rogers 2019 for a comprehensive review). In MESA, angular momentum transport is modelled in a fully diffusive scheme. Note that this approach inadequately models the meridional currents,[16] which are an advective process by nature. MESA solves the angular momentum transport equation following equation (46) of Heger, Langer & Woosley (2000), which is based on the works by Endal & Sofia (1978) and Pinsonneault et al. (1989), that is:

$$\frac{\partial \Omega}{\partial t} = \frac{\partial}{\partial m}\left[(4\pi r^2 \rho)^2 \, D_{\rm AM} \, \frac{\partial \Omega}{\partial m}\right], \tag{11}$$

where $D_{\rm AM}$ is the total diffusion coefficient responsible for angular momentum transport, while r, ρ, and m are the radius, density, and enclosed mass, respectively, and t is the time.

In the non-magnetic models, we assume that $D_{\rm AM}$ is constructed as a sum of four diffusion coefficients (resulting from dynamical and secular shear, meridional circulation, and GSF instability), which are the same as used for the Mix1 chemical mixing scheme in equation (16); however, not scaled by any efficiency parameters for angular momentum transport. For simplicity and a consistent treatment of angular momentum transport, we also use these diffusion coefficients for angular momentum transport when a different chemical mixing scheme is adopted (Mix2, see below).

In the INT models (see also Fig. 1), we assume that the magnetic field is capable of establishing radially uniform (solid-body) rotation throughout the entire star. This is representative of an axisymmetric magnetic field that 'freezes' rotation along the poloidal field lines following Ferraro's theorem (Ferraro 1937). We model this by using the MESA controls `set_uniform_am_nu_non_rot = .true.` and `uniform_am_nu_non_rot = 1.d16` such that a high diffusivity ($D_{\rm AM} = 10^{16}$ cm^2 s^{-1}) leads to efficient angular momentum transport and hence solid-body rotation throughout the entire star. Unfortunately, the naming conventions here are somewhat confusing as these controls are applied to the entire star regardless of the convective/radiative nature of given layers. Otherwise 'am_nu_non_rot' refers to layers of the star with convective mixing. The precise value of this quantity is not crucial so long as it achieves solid-body rotation. Above a critical value, the diffusivity can saturate, meaning that an already flat Ω profile will remain unchanged if an even higher diffusivity is applied. The MESA 'default' value for this control is $D_{\rm AM} = 10^{20}$ cm^2 s^{-1}. Such a high diffusivity would mean a diffusion time-scale ($\tau_{\rm D} \approx r^2/D_{\rm AM}$) of a few hours, which is physically not justified. The saturation, i.e. solid-body rotation for a given diffusivity may happen for diffusivities $>10^{10}$ cm^2 s^{-1}, depending on model specifics such as mass and evolutionary stage.

In the SURF models, we distinguish between three regions of the star (i) the stellar core, (ii) the envelope from $q = 0.8$ to the stellar core, and (iii) the envelope above $q = 0.8$ in which magnetic braking is applied (see above). On the main sequence, the cores of massive stars are convective, dominated by strong turbulent mixing. In MESA, this is modelled by a high diffusion coefficient (relying on mixing-length theory) that establishes a constant angular velocity profile, that is, the core is rigidly rotating. In the radiative layers between the stellar core and the boundary of $q = 0.8$, the usual hydrodynamical instabilities (dynamical and secular shear, meridional circulation, GSF instability) transport angular momentum. More directly, the assumption here is that there is no magnetic coupling between the stellar core and the envelope. While even for complex surface fields there may be weak dipole components in the deep stellar layers which may contribute to angular momentum transport, we neglect those here to be able to test a limiting, boundary case, in which differential rotation may develop between the core and the surface. For a consistent comparison, in both Mix1/Mix2 chemical mixing schemes (see below), we apply the same treatment of angular momentum transport in this region.

The fossil magnetic field may relax into a non-axisymmetric configuration, strongly impacting the upper stellar layers (Braithwaite 2008). In these layers (with 20 per cent of the stellar mass in our models), we apply a high diffusion coefficient of $D_{\rm AM} = 10^{16}$ cm^2 s^{-1} via the `other_am_mixing` subroutine to account for the expected effect of the magnetic field.

In both INT and SURF cases, for layers with increased angular momentum transport attributed to the magnetic field, the angular momentum transport equations are of secondary importance in the sense that we expect an appropriate transport equation to result in a flat angular velocity profile, thereby deviating from non-magnetic models. One would also expect that in those layers where the fossil magnetic field is present, hydrodynamical instabilities could not transport angular momentum.

Further guidance regarding the internal rotation profile and magnetic field properties can also be obtained observationally using (magneto-)asteroseismology (see recently Lecoanet, Bowman & Van Reeth 2022). For instance, radial differential rotation was observed in several massive stars using the rotational splitting of gravity modes (e.g. Aerts et al. 2003; Triana et al. 2015). On the other hand, the nearly identical surface and core rotation of red giant stars requires very efficient transport (e.g. Moyano et al. 2022). Using asteroseismic analysis of *Kepler* data, it has indeed been attributed to magnetic fields (Fuller et al. 2015). Due to possible mode suppression by strong magnetic fields, magnetoasteroseismology remains an elusive target, having been performed for only a few massive stars (e.g. HD 43317 and V2052 Oph; Briquet et al. 2012; Buysschaert et al. 2018). However, the advent of nearly all-sky high-precision space-based photometry can help further this line of inquiry, with large asteroseismic target lists of OB stars already being assembled (e.g. Burssens et al. 2020).

2.7 Rotational mixing of chemical elements

Following Pinsonneault et al. (1989), rotational mixing of chemical elements is commonly applied via the diffusion equation in 1D stellar evolution models:

$$\frac{\partial X_i}{\partial t} = \frac{\partial}{\partial m}\left[(4\pi r^2 \rho)^2 \, D_{\rm chem} \, \frac{\partial X}{\partial m}\right] + \left(\frac{{\rm d}X_i}{{\rm d}t}\right)_{\rm nuc}, \tag{12}$$

[16] Meridional currents are large-scale flows arising from the thermal imbalance between the polar axis and the equatorial regions in a rotating star.

where X_i is the mass fraction of a given element i, t is the time, m and ρ are the mass coordinate and mean density at a given radius r, $D_{\rm chem}$ is the sum of individual diffusion coefficients contributing to chemical mixing (see also Salaris & Cassisi 2017), and the last term accounts for nuclear burning.

In this approach, the central question is how to encapsulate inherently 3D physical processes and apply them via a single parameter $D_{\rm chem}$. In this study, we contrast two commonly used approaches. Spectroscopic studies of massive stars often find discrepancies between the observed and predicted surface abundances from rotating stellar evolution models computed with a given scheme of chemical mixing (e.g. Trundle et al. 2004; Martins et al. 2017; Markova, Puls & Langer 2018). Recent works suggest that such discrepancies may be resolved by including additional processes in the calculations, for example, internal gravity waves (and magnetic fields) lead to a more complex physical interplay between various processes and a variety of mixing profiles (Aerts et al. 2019; Bowman et al. 2020; Michielsen, Aerts & Bowman 2021; Pedersen et al. 2021).

2.7.1 *Basic thermodynamic quantities*

Before introducing the diffusion coefficients, we briefly outline the most important thermodynamic quantities that enter into those equations. The thermal diffusivity is defined as:

$$K = \frac{4ac}{3\kappa}\frac{T^4\nabla_{\rm ad}}{\rho P\delta} = \frac{4acT^3}{3\kappa\rho^2 c_P}\,, \tag{13}$$

where a is the radiation constant, c the speed of light, κ the mean radiative opacity, c_P the specific heat capacity per unit mass at constant pressure, T the temperature, ρ the density, and P the pressure. The different ∇-s below denote the advective, radiative, and chemical composition (μ) gradients:

$$\begin{aligned}
\nabla_{\rm ad} &= \left(\frac{\partial \ln T}{\partial \ln P}\right)_{S,\mu} = \frac{P\delta}{T\rho c_P}\\
\nabla_{\rm rad} &= \left(\frac{\partial \ln T}{\partial \ln P}\right)_{\rm rad} = \frac{3}{16acG}\frac{\kappa L P}{mT^4}\\
\nabla_{\mu} &= \frac{\partial \ln \mu}{\partial \ln P}\,,
\end{aligned} \tag{14}$$

where S is the entropy, μ the mean molecular weight, and G the gravitational constant. The local luminosity L is the rate of energy transported outward through a sphere of radius r, and m is the enclosed mass. From equation (4.22) of Maeder & Zahn (1998), the derivatives from the equation of state are:

$$\begin{aligned}
\delta &= -(\partial \ln \rho/\partial \ln T)_{P,\mu}\\
\phi &= (\partial \ln \rho/\partial \ln \mu)_{P,T}\,.
\end{aligned} \tag{15}$$

2.7.2 *Mix1 scheme*

A commonly used scheme of rotational mixing in stellar evolution models was developed by Kippenhahn (1974), Endal & Sofia (1978), and Pinsonneault et al. (1989) and applied subsequently by several authors. This scheme (the 'default' MESA scheme, 'Mix1' hereafter) is typically used in MESA models (e.g. Paxton et al. 2013; Choi et al. 2016). $D_{\rm chem}$ is constructed as the sum of six individual diffusion coefficients, describing dynamical shear instability (DS), Solberg–Høiland instability (SH), secular shear instability (SS), Goldreich–Schubert–Fricke instability (GSF), Eddington–Sweet circulation (ES), and Tayler–Spruit dynamo (ST) (see Eddington 1925; Solberg 1936; Høiland 1941; Sweet 1950; Goldreich & Schubert 1967; Fricke 1968; Tayler 1973; Endal & Sofia 1978; Pinsonneault et al. 1989; Spruit 2002)

To be able to compare our results to common model grids, in the Mix1 scheme we adopt the diffusion coefficient applied in equation (12) as:

$$D_{\rm chem}^{\rm Mix1} = f_{\rm c}(D_{\rm ES} + D_{\rm SS} + D_{\rm DS} + D_{\rm GSF}), \tag{16}$$

where the individual diffusion coefficients are described according to Heger et al. (2000). Transport by dynamo mechanisms and by the Solberg–Høiland instability are not considered as their contribution to chemical mixing has been debated (e.g. Yoon et al. 2006; Brott et al. 2011a). Of particular interest is the meridional circulation term, which was described via the circulation velocity in the radial direction by Kippenhahn (1974) and constructed into a diffusion coefficient by Endal & Sofia (1978). However, the base formulation of the problem in terms of a steady-state circulation by Vogt (1925), Eddington (1925), and Sweet (1950) has been disputed by, e.g. Busse (1981,1982), Zahn (1992) – see further discussion by Rieutord (2006).

The simple summation of the various processes by Heger et al. (2000, 2005) is often criticised on theoretical grounds as the various processes are not independent of one another (e.g. recently Chang & Garaud 2021, and references therein). For example, the dynamical and secular shears act on different time-scales, and therefore their mutual use is physically contradictory. Maeder et al. (2013) proposed a diffusion coefficient accounting for the interactions between the different physical processes. While several studies have scrutinised these instabilities and resulting diffusion coefficients (e.g. Caleo, Balbus & Tognelli 2016; Barker, Jones & Tobias 2019, 2020; Goldstein et al. 2019; Chang & Garaud 2021; Park et al. 2021, and references therein), a unified description of instabilities in rotating stars is still not fully complete.

In fully diffusive approaches as described above, two arbitrary scaling factors $f_{\rm c}$ and f_μ, introduced by Pinsonneault et al. (1989), are commonly adopted. If chemical gradients ∇_μ (equation 14) develop, they may inhibit the efficiency of mixing. This is primarily due to ∇_μ serving as a stability criterion for the development of rotational instabilities (see e.g. Maeder 1997) since it appears directly in several of the individual diffusion coefficients used in equation (16). To alter the effect of chemical gradients on mixing, the scaling factor f_μ is introduced such that ∇_μ is replaced by $f_\mu \cdot \nabla_\mu$ when calculating stability criteria for various instabilities.

The parameter $f_{\rm c}$, multiplying all individual diffusion coefficients in equation (16), was first calibrated to $f_{\rm c} = 0.046$ by Pinsonneault et al. (1989). This reduction in the efficiency of chemical mixing (compared to angular momentum transport) was needed to explain the observed lithium depletion in the Sun. However, recent studies (e.g. Prat et al. 2016) found that, at least, for the shear instability, both chemical mixing and angular momentum transport should have similar efficiencies when using the same diffusion coefficient.

Heger et al. (2000) found that $f_{\rm c} = 0.033$ with $f_\mu = 0.05$ (which were the default MESA options until recently) best reproduce the observed nitrogen enrichment in the 10–20 $M_\odot$ mass range at Solar metallicity.[17] Yoon et al. (2006) concluded that when the angular momentum transport is very efficient (by using the magnetic term $D_{\rm ST}$ accounting for the Tayler–Spruit dynamo), then $f_{\rm c} = 0.033$ should be used with $f_\mu = 0.1$ instead of $f_\mu = 0.05$. Using similar physical

[17] Heger et al. 2000 also comment that for an initial rotation of 200 km s^{-1} and fixed $f_c = 0.033, f_\mu \geq 0.25$ is inconsistent with observations in the 30–60 $M_\odot$ mass range.

assumptions as Heger et al. (2000) and Yoon et al. (2006), Brott et al. (2011a) calibrated $f_c = 0.0228$ for a 13 $M_\odot$ model based on the surface enrichment of early B stars in the LMC[18] and adopted $f_\mu = 0.1$ from Yoon et al. (2006). Recently, Markova et al. (2018) found that this calibration produces insufficient mixing for more massive stars to be compatible with observations. Some subsequent modelling approaches even adopt a mixing efficiency parameter f_c that is a factor of 10 higher (Aguilera-Dena et al. 2020).

When using similar physics (assuming a purely diffusive equation to model angular momentum transport), Chieffi & Limongi (2013) obtained calibrations for $f_c = 0.07$ with $f_\mu = 0.03$ and $f_c = 0.2$ with $f_\mu = 1.0$ (correctly noting the degeneracy between these parameters). They also performed calibrations with different physics (using the advecto-diffusive equation of angular momentum transport) which yielded $f_c = 1$ with $f_\mu = 0.03$ for chemical mixing. Recently, also using a physical approach different from the above mentioned ones, Costa et al. (2019) used intermediate-mass binary systems and constrained $f_c = 0.17$ with $f_\mu = 0.47$.

To be able to compare to previous works which used the same physics, we adopt $f_c = 0.033$ and $f_\mu = 0.1$ (`am_D_mix_factor` = 0.033, `am_gradmu_factor` = 0.1) when using the Mix1 scheme.[19]

2.7.3 Mix2 scheme

Another commonly used mixing scheme ('Mix2' hereafter) was developed by Zahn (1992), Chaboyer & Zahn (1992), Maeder (1997), Maeder & Zahn (1998), Maeder & Meynet (2000). This scheme has been applied in the Geneva stellar evolution code (GENEC, Eggenberger et al. 2008; Ekström et al. 2012; Georgy et al. 2013; Meynet et al. 2013; Groh et al. 2019; Keszthelyi et al. 2019; Murphy et al. 2021), as well as in modelling approaches using the ROSE (Potter, Tout & Eldridge 2012a; Potter et al. 2012b) and FRANEC codes (Chieffi & Limongi 2013). Here, we adopt it in MESA, which treats angular momentum transport in a fully diffusive scheme, unlike the above mentioned approaches. Therefore, a direct comparison to previous works is not possible. The major difference is that given the efficient diffusive angular momentum transport, strong shear mixing cannot develop. Consequently, in our models with the Mix2 scheme, the main chemical element transport is via meridional currents during most of the main sequence evolution. This is not the case in the models of Ekström et al. (2012), where the advective treatment of angular momentum transport allows for shears, which may also become the dominant process of transporting chemical elements. As we will see (Section 3.1, Section E), the Mix2 scheme leads to quasi-chemically homogeneous evolution for the entire main sequence of our non-magnetic models. Since such a behaviour is expected to be rare, we may consider the adaptation of this mixing scheme in our models as a limiting case for very efficient mixing.

The effective diffusion coefficient for chemical mixing combines the effects of meridional currents and horizontal turbulence,

$$D_{\rm eff} = \frac{1}{30}\frac{|\,rU(r)|^2}{D_h}\,, \tag{17}$$

where the radial component of the meridional circulation is

$$U(r) = \frac{P}{\rho g C_P T}\quad \frac{1}{\nabla_{\rm ad} - \nabla_{\rm rad} + \frac{\phi}{\delta}\nabla_\mu} \times \left(\frac{L}{M'}[E^\star_\Omega + E_\mu] + \frac{c_P}{\delta}\frac{\partial \vartheta}{\partial t}\right), \tag{18}$$

with P the pressure, ρ the density, g the gravitational acceleration, T the temperature, L the luminosity, $M' = M_\star(1 - \Omega^2/2\pi g\rho_{\rm m})$, $E^\star_\Omega$ and E_μ terms which depend on the distribution of angular velocity and mean molecular weight,[20] and ϑ the ratio of the variation of the density to the mean density $\rho_{\rm m}$. The horizontal turbulence is adopted as:

$$D_h = \frac{1}{c_h}\, r\, |2V(r) - \alpha U(r)|\,, \tag{19}$$

where $c_{\rm h}$ is a constant set to unity (see Chaboyer & Zahn 1992), and $V(r)$ expresses the radial dependence of the horizontal component of the meridional circulation. The horizontal component is expressed as $V(r)P2(\cos\Theta)$, where $P2$ is the second Legendre polynomial and Θ is the co-latitude. We set $V(r) = U(r)$ as a reasonable approximation. Then,

$$\alpha = \frac{1}{2}\frac{{\rm d}\ln(r^2\Omega)}{{\rm d}\ln r}\,. \tag{20}$$

The diffusion coefficient accounting for vertical shear mixing is derived by Maeder (1997) as:

$$D_{\rm shear} = f_{\rm energ}\frac{H_P}{g\delta}\frac{K}{\left[\frac{\phi}{\delta}\nabla_\mu + (\nabla_{\rm ad} - \nabla_{\rm rad})\right]}\left(\frac{9\pi}{32}\,\Omega\,\frac{{\rm d}\ln\,\Omega}{{\rm d}\ln\,r}\right)^2\,, \tag{21}$$

where $f_{\rm energ}$ is a free parameter set to unity. H_P is the local pressure scale height, g the gravitational acceleration, Ω the angular velocity, and r the radius. Finally, in the Mix2 scheme, the diffusion coefficient applied in equation (12) is:

$$D^{\rm Mix2}_{\rm chem} = D_{\rm eff} + D_{\rm shear}\,. \tag{22}$$

In this case, the free parameters f_c and f_μ are not used in GENEC calculations. Consequently, we do not apply them in our MESA Mix2 model calculations either (`am_D_mix_factor` = 1, `am_gradmu_factor` = 1). To our knowledge this mixing scheme is implemented in MESA for the first time. The sum of diffusion coefficients, dominated by meridional currents ($D_{\rm eff}$, equation (17)) in the solid-body rotating case are comparable in shape to the default MESA approach which uses $D_{\rm ES}$ as derived by Kippenhahn (1974) and Pinsonneault et al. (1989). However, the amplitudes are not equal (as shown in Fig. 3).

We note here that there is some confusion in the literature regarding the work of Chaboyer & Zahn (1992). Heger et al. (2000) (and following publications) state that Chaboyer & Zahn (1992) found $f_c = 1/30$ based on a theoretical approach. The work of Chaboyer & Zahn (1992) does not introduce any scaling factors. $D_{\rm eff}$, describing the transport resulting from the interaction between meridional currents and the strong horizontal turbulence is obtained by integrating the equation for the transport of chemical elements over latitudes. This integration gives rise to the numerical term of 1/30 (in their equation (16) and our equation (17)), resulting from the decomposition of the meridional velocity in Legendre polynomials.

[18] These values were also adopted for their Solar and SMC models.

[19] We note that presently there is a growing amount of evidence that such a reduction in the efficiency of chemical mixing caused by hydrodynamical instabilities is likely not needed at all. Instead, there exist other processes that are simply more efficient in transporting angular momentum than chemical elements, the prime candidates being internal gravity waves and internal magnetic fields (e.g. Aerts et al. 2019, and references therein).

[20] The full expression of these terms is given by Maeder & Zahn (1998). In our approach, we simplify this expression and adopt only the leading term which is the first term of $E^\star_\Omega$ as described by Maeder & Zahn (1998). Since it is a smaller term, we set E_μ to zero.

This is not a scaling factor to match observations and it does not apply to any other diffusion coefficient. Similarly, in equation (9) the numerical term 2/3 is not an arbitrary scaling factor that one would tailor to observations.

3 RESULTS

In this section, we first consider non-magnetic models, and then a fiducial model with $M_{\rm ini} = 20\ {\rm M}_{\odot}$, $\Omega_{\rm ini}/\Omega_{\rm crit,\ ini} = 0.5$, $Z_{\rm ini} = 0.014$, and $B_{\rm eq,\ ini} = 3$ kG within the INT/Mix1 scheme, and follow changes in its stellar structure and evolution. In particular, we will first vary the mixing and braking schemes to investigate the impact on stellar structure models in Section 3.1.1 and abundances in Section 3.1.2 and in evolutionary models in Section 3.2.1. Then, a typical HRD evolution of the INT and SURF magnetic models in the full mass range (3–60 $\rm M_{\odot}$) will be addressed in Section 3.2.2, followed by predictions for the Kiel diagram in Section 3.2.3. Nitrogen abundances and other schemes are also shown in Appendix E (Supplementary). Finally, the initial magnetic field strength and metallicity will be varied within the evolutionary models in Sections 3.2.5 and 3.2.6.

3.1 Stellar structure models

3.1.1 Chemical mixing and angular momentum transport

Figs 2, 3, and 4 show 20 $\rm M_{\odot}$ models at solar metallicity. These structure models are at half-way through their core hydrogen burning phase[21] (defined as $X_{\rm core}/X_{\rm core,\ init} = 0.5$). In Fig. 2, we show non-magnetic models in the Mix1 (top panel) and Mix2 (lower panel) chemical mixing schemes. (Since magnetic braking is not applied, there is no braking scheme in these cases, hence we refer to these models as 'NOMAG'.) In Fig. 3, the fiducial model (INT/Mix1, top panel) as well as an otherwise initially identical model but within the INT/Mix2 scheme (lower panel) is shown. Models with the SURF/Mix1 and SURF/Mix2 schemes are shown in Fig. 4. Note that the models with the adopted braking and mixing schemes correspond to different stellar ages when the core hydrogen is half-way depleted in each model (indicated in the title of the panels), given the different evolution resulting from the change in physical assumptions.

When fossil magnetic fields are not considered in the models (NOMAG case; $B_{\rm eq} = 0$), the Mix1 and Mix2 chemical mixing schemes produce drastically different results. In the Mix1 scheme, the mean molecular weight (shown with magenta line and on the right ordinate) drops rapidly at the convective core boundary (the zones with convective overshooting are shown with orange in Fig. 2). Near this region the GSF instability dominates (see e.g. the recent studies of Caleo et al. 2016; Barker et al. 2019, 2020; Chang & Garaud 2021). Once the chemical composition is stabilised, meridional circulation drives chemical mixing (red line) and angular momentum transport (dotted line). Note that the assumption of $f_{\rm c} = 0.033$ reduces the efficiency of all instabilities considered for chemical mixing compared to the efficiency of the same instabilities used for angular momentum transport. The angular velocity profile (right-hand panel) remains completely flat in the stellar envelope, with a small break at the core boundary. Thus the model is very close to solid-body rotation. The NOMAG/Mix2 model reveals a very efficient mixing, with an almost flat mean molecular weight profile indicating close-to chemically homogeneous evolution. The dominant transport is via the effective diffusion coefficient (equation 17). Importantly, the diffusion coefficients at the core-envelope boundary are smooth. This is a critical region that allows for mixing up material from the core to the surface. Note the much larger convective core (in grey) compared to the Mix1 model. The specific angular momentum (blue line, right-hand panel) and angular velocity profiles are smooth throughout the star. Ω slightly decreases near the surface as a result of mass loss, however, this model is also very close to solid-body rotation.

In the INT braking scheme (Fig. 3) the angular velocity profile is completely flat. The star is rigidly rotating due to the assumed high diffusivity for transporting angular momentum attributed to the magnetic field, albeit the angular rotation is much lower than in the NOMAG model due to magnetic braking (uniformly) lowering the specific angular momentum. The rigid rotation does not allow shears to develop and transport angular momentum or chemical elements. Therefore in these models the chemical enrichment is entirely driven by meridional currents. In the 'standard' MESA description (Mix1 scheme) a gap in the transport develops above the overshooting region, corresponding to steep chemical gradients, as seen from the large drop of the mean molecular weight (magenta line, right ordinate) at the core boundary. Despite the mitigating effect of $f_{\mu} = 0.1$ in these models, the inefficient mixing above the core boundary will prevent a very efficient surface enrichment and overall mixing inside the star. If the gap existed throughout the entire early evolution, it would completely inhibit surface enrichment. However, the gap is not present initially – see top panels of Figs D1 and D2 (Supplementary) – when the mixing and corresponding enrichment are prominent. With internal magnetic braking, all layers of the star lose angular momentum, therefore the shape of the specific angular momentum profile remains unchanged whereas its overall value decreases over time. In the Mix2 scheme, $D_{\rm eff}$ never becomes zero close to the convective core. This allows for a smoother composition gradient and more overall mixing, therefore differences in surface abundances are expected. On the other hand, the specific angular momenta are not so different between the Mix1 and Mix2 schemes in the INT models. Ω is smaller in the Mix2 model, but this quantity also depends on the radius of the star. Since the model in the INT/Mix2 scheme takes more time than the INT/Mix1 to deplete hydrogen in its core due to the more efficient chemical mixing, at half-way through its core burning stage it has a larger radius. We also note that the NOMAG/Mix2 model produces a more efficient mixing than the INT/Mix2 model. As a consequence, the INT/Mix2 model results in a smaller convective core than the non-magnetic case.

In the SURF braking scheme (Fig. 4), one major difference is that there is no overall solid-body rotation. Let us recall that in the SURF models only the outer layers enclosing the top 20 per cent of the total mass of the star are assumed to lose angular momentum (see equation 10) and have an increased diffusivity for angular momentum transport (via equation 11). In a 1D diffusive scheme, angular momentum flows from inner to outer layers. The angular velocity profile is flat in those layers where the diffusivity is increased. Depending on the mixing scheme, the composition and also the mixing processes are rather different. The magnitude and radial dependence of the diffusion coefficient for angular momentum transport also determines the angular velocity in the rest of the stellar envelope. We see that in the SURF/Mix1 model the angular velocity is also roughly constant between 0.6 and 0.8 $m/M_{\star}$, and it gradually changes closer to the boundary of the stellar core, as it is the case for $D_{\rm AM}$ (left-hand panel, dotted line). In the SURF/Mix2 model, $D_{\rm AM}$ changes more abruptly at around 0.8 $m/M_{\star}$, whereas it is roughly constant again closer to the stellar core. Braking for a given magnetic field strength is less efficient in the SURF scheme than in the INT

[21] The ZAMS and TAMS structure models of the four schemes are shown in Figs D1–D4 in the Appendix (Supplementary).

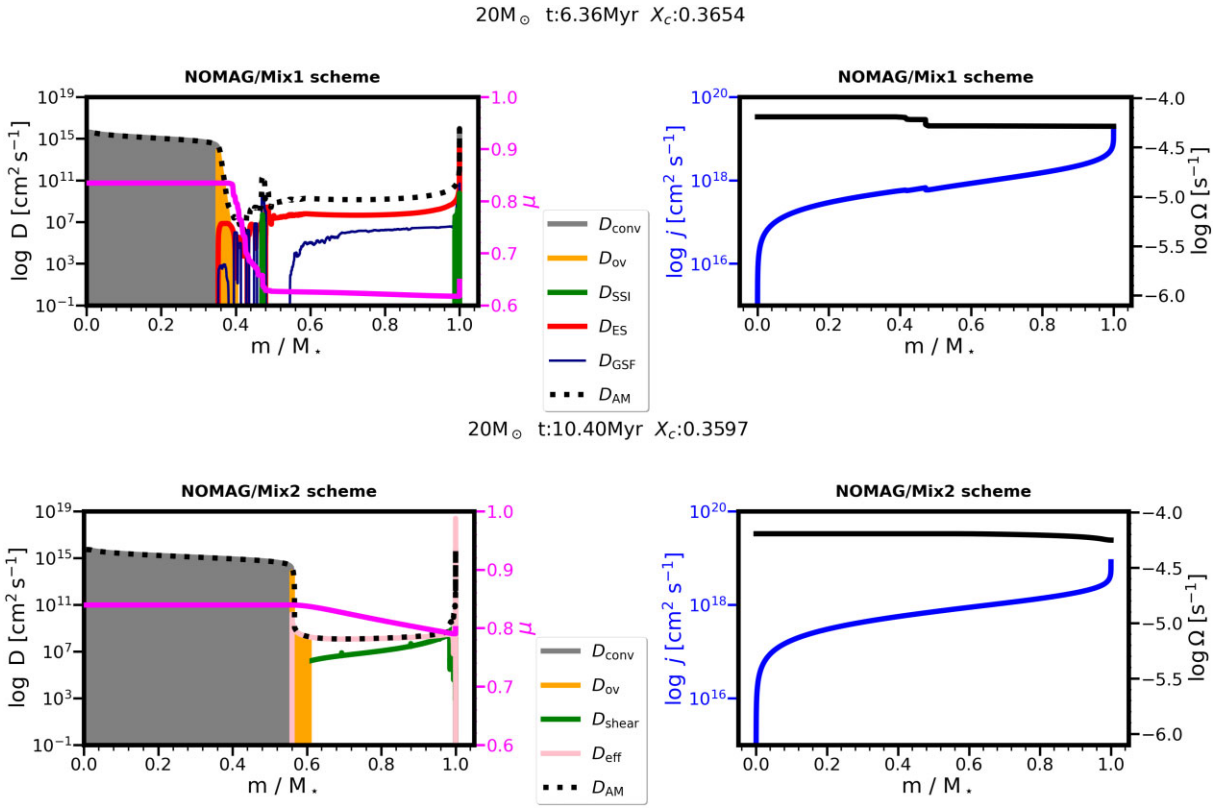

Figure 2. We show a non-magnetic model of $M_{\rm ini} = 20\,{\rm M}_{\odot}$ (at $Z = 0.014$) within the NOMAG/Mix1 scheme (top panel) and an initially identical model within the NOMAG/Mix2 scheme (lower panel) at half-way through its core hydrogen burning phase (with core hydrogen mass fraction of $X_{\rm c}/X_{\rm c,init} \approx 50$ per cent). Left-hand panel: diffusion coefficients for chemical mixing (solid lines for rotational mixing and shaded grey and orange for convective core mixing and overshooting, respectively; all entering via $D_{\rm chem}$ in equation 12) and diffusion coefficient for angular momentum transport (dotted line, entering equation 11). The right ordinate and magenta line show the mean molecular weight. Due to the stochastic nature of mixing processes and, in some cases, numerical noise, here and hereafter we apply a moderate smoothing of some diffusion coefficients for visualisation purposes. Right-hand panel: Specific angular momentum (left ordinate, blue line) and angular velocity (right ordinate, black line).

scheme since the Alfvén radius is smaller for a quadrupole field than for a dipole field as defined by equations (3)–(5). Given the shape of the specific angular momentum profile (right-hand panel, blue line), the SUFR/Mix1 model has a break closer to the stellar core, while the SURF/Mix2 model has a break closer to 0.8 $m/M_{\star}$. This means that the SURF/Mix2 model can more easily exhaust its surface reservoir of angular momentum.

Certainly, further research is required to investigate how angular momentum transport and magnetic braking work for more complex magnetic field configurations and how they could be implemented in 1D stellar evolution models. Overall, the results from the SURF approach may be considered similar to the works of Meynet et al. (2011) and Paper I , where magnetic braking was only applied to the uppermost stellar layer.

In the SURF/Mix1 scheme, the GSF instability can efficiently transport chemical elements near the core boundary. This instability acts on a dynamical time-scale and therefore can vary from time-step to time-step. In the upper envelope meridional currents remain efficient. In the Mix2 scheme, the free parameters controlling mixing efficiency are not applied ($f_{\mu} = 1, f_{\rm c} = 1$), and the SURF/Mix2 scheme is thus the most efficient in chemical mixing. This is also evidenced by the larger convective core size compared to the three models in the other magnetic schemes. In fact, the convective core size of the SURF/Mix2 model is similar to that of the NOMAG/Mix2 model. Strong gradients of chemical elements do not develop near the core boundary. Shear mixing remains efficient in the entire envelope to transport chemical elements.

3.1.2 Abundances of He, C, N, O

Fig. 5 shows the abundances of helium, carbon, nitrogen, and oxygen. For three models (INT/Mix1, INT/Mix2, SURF/Mix1) the convective hydrogen core sizes are comparable. The SURF/Mix2 scheme, which is the most efficient in mixing, leads to a much larger core. In this model, the average helium content in the stellar envelope is much higher and the surface will also show this increased abundance already on the main sequence. Carbon is slightly depleted during the CNO-cycle (it becomes most depleted in a thin layer close to the core boundary), however the surface carbon abundance is minimally changed in the first three models. In contrast, the SURF/Mix2 model produces an almost uniform distribution of carbon inside the star, it is completely mixed in the envelope without any gradients. Nitrogen excess is produced during the CNO-cycle, and therefore, its surface abundance is a crucial measurement to infer the efficiency of internal mixing. All models produce a surface nitrogen enrichment, except the INT/Mix1 scheme. Here a strong gradient develops between the core and the surface. While a core-surface gradient is also present in the INT/Mix2 and SURF/Mix1 models, their envelopes have a somewhat higher mean nitrogen abundance and their surfaces are slightly enriched in nitrogen. The SURF/Mix2 model has an almost homogeneous nitrogen distribution in its envelope. Oxygen is depleted during the CNO-cylce. Similar to carbon, oxygen can still remain abundant in the envelope in the first three models. The SURF/Mix2 model yields a close-to-homogeneous oxygen distribution throughout the star. In contrast to carbon, in all four

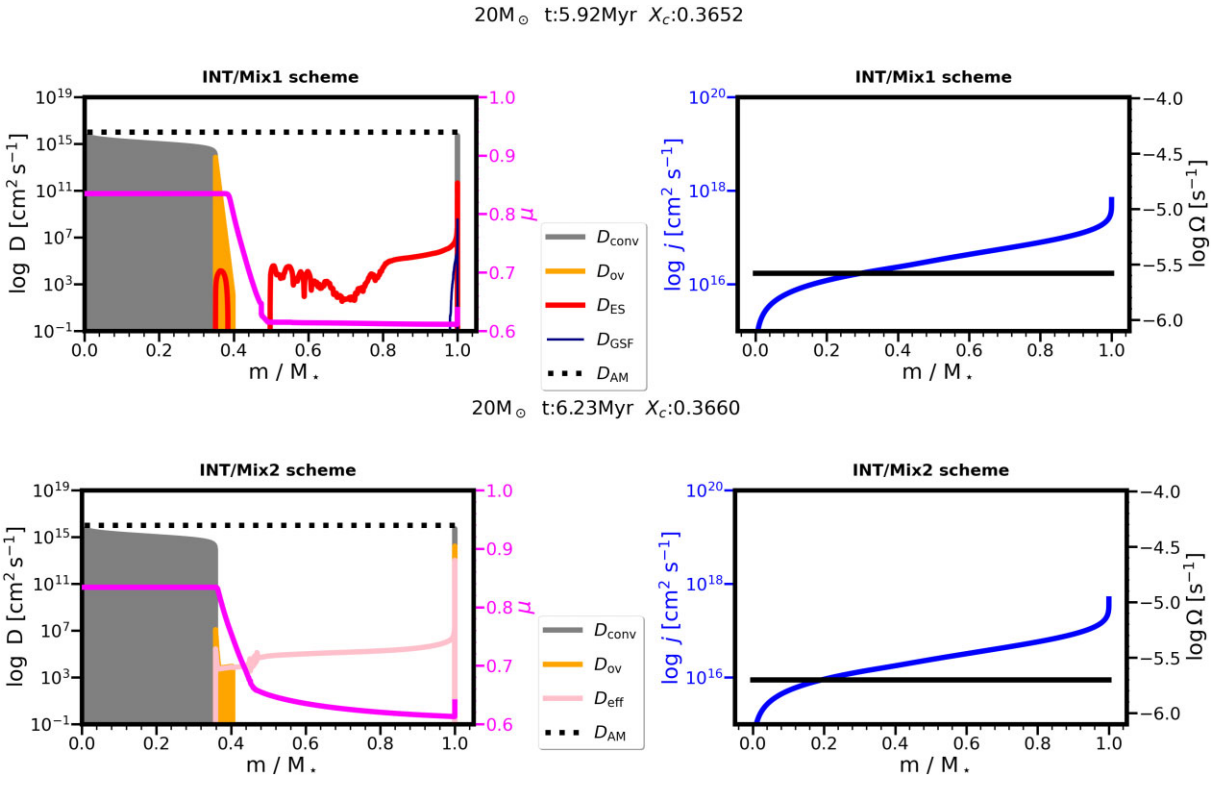

Figure 3. Same as Fig. 2 but for magnetic models within the INT magnetic braking scheme.

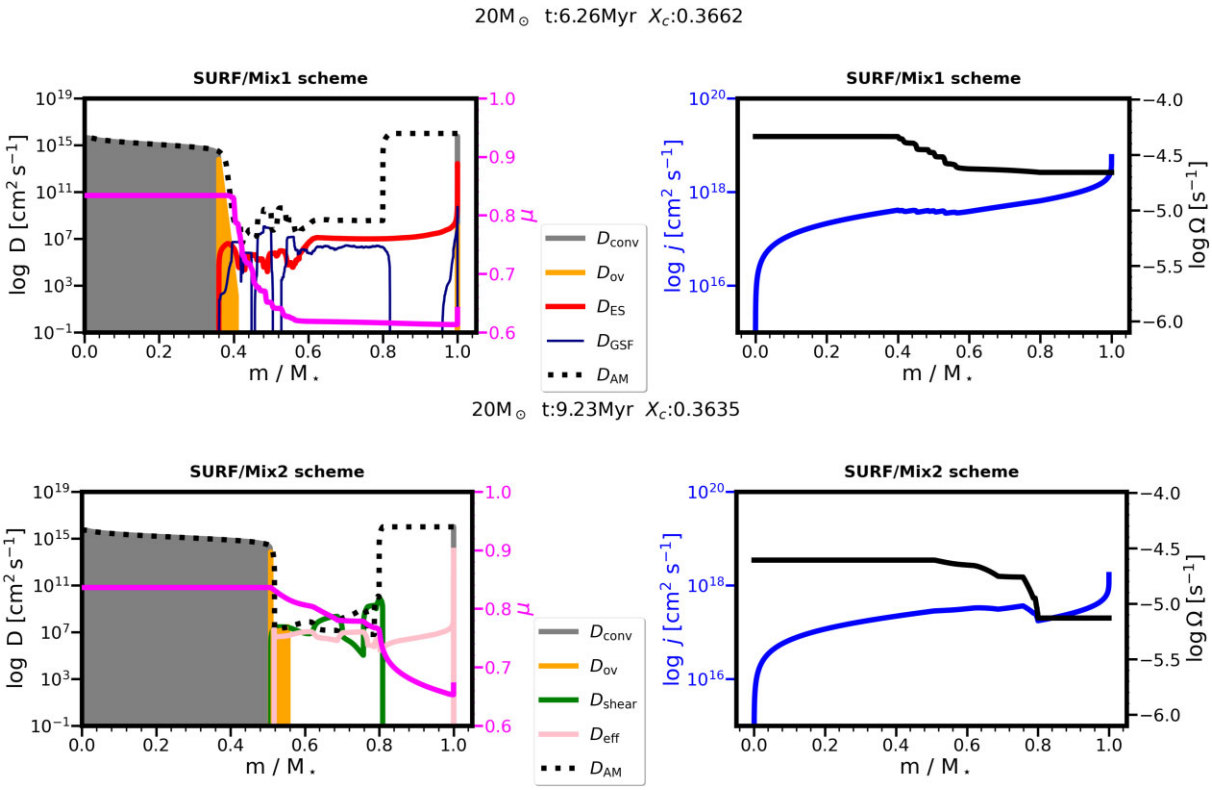

Figure 4. Same as Fig. 2 but for magnetic models within the SURF magnetic braking scheme.

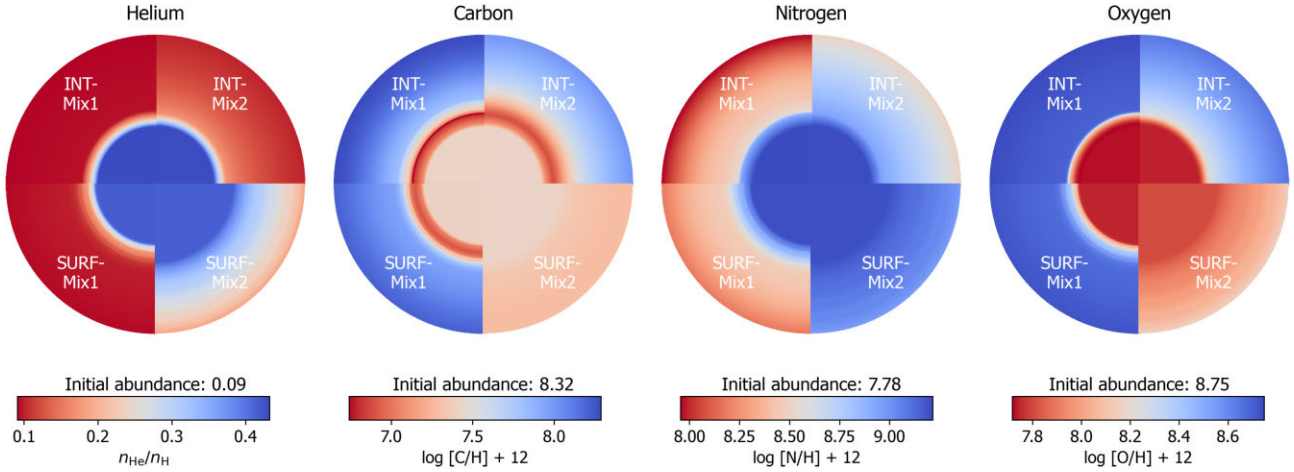

Figure 5. He, C, N, and O abundances for the same models as in Figs 3 and 4 at $X_c \approx 0.36$. In each circle, colour maps show the abundance of one element as a function of stellar mass coordinate, where the distance from the centre of the circle corresponds linearly to the mass enclosed within that radius. Each quarter circle contains the abundance profiles of one model. He abundance is in number fraction, the other elements in logarithmic number fractions. These profiles are prepared using TULIPS (Laplace 2021).

models oxygen is depleted in the entire stellar core. For example, the core to surface oxygen abundance can differ by an order of magnitude in the INT/Mix1 model.

The reason why strong gradients can develop (and remain in most models) near the core boundary is related to the drop in chemical mixing, identifiable by drops and gaps in the diffusion coefficients (c.f. Figs 3–4), which in turn depend on the composition gradients. The velocity of the diffusion is zero when there is no composition gradient and it increases when the gradient increases. This is another effect that leads to reducing the diffusion coefficient. For helium, the difference between the core and the envelope grows gently, while for nitrogen it grows faster because nitrogen is enhanced very rapidly in the core. Thus for a given diffusion coefficient, nitrogen will diffuse more rapidly than helium. In the Mix2 scheme, the key differences between the INT and SURF models result from their different angular velocity profiles. The INT models lose angular momentum in all layers and thus mixing becomes less efficient overall. The SURF/Mix2 model has a more massive convective core at the same evolutionary stage (c.f. Fig. 4), and the envelope closely reflects on the core composition as this model has an almost homogeneous distribution of chemical elements. In both INT/Mix1 and INT/Mix2 schemes, envelope mixing has a similar overall efficiency. However, in the INT/Mix2 scheme, the near core mixing is more efficient (see above), greatly impacting the measurable surface abundances of carbon, nitrogen, and oxygen. The surface abundances, especially of nitrogen, are sensitive to the chosen braking and mixing schemes, especially with the Mix2 scheme reflecting more closely the core composition than the Mix1 scheme.

3.2 Evolutionary tracks

3.2.1 Impact of magnetic braking and chemical mixing schemes for 20 $M_\odot$ models

Fig. 6 shows the fiducial 20 $M_\odot$ model (INT/Mix1) as well as initially identical models but in the other three schemes in the HRD, Kiel diagram, and Hunter diagram[22] (Hunter et al. 2008, 2009). Here we address the impact of using the different braking and mixing schemes for otherwise identical models with the same initial mass and initial magnetic field strength.

The models within the Mix1 chemical mixing scheme result in closely overlapping tracks on the HRD and Kiel diagrams. However, as evidenced from the Hunter diagram (right-hand panel of Fig. 6), the spin-down and chemical enrichment are different when considering the different magnetic braking schemes. The 20 $M_\odot$ INT/Mix1 model (solid line) produces essentially no observable surface nitrogen enrichment in this configuration. The SURF/Mix1 model (dashed-dotted line), on the other hand, maintains a higher angular velocity in the inner regions of the star by braking only the upper layers (see Section 3.1). This is why mixing remains more efficient and a larger amount of nitrogen is mixed to the stellar surface (0.45 dex). Model predictions within the Mix2 chemical mixing scheme produce a much more efficient chemical mixing than the Mix1 scheme. However, the differences between the INT/Mix2 and INT/Mix1 schemes are relatively modest on the HRD and Kiel diagrams, while the Hunter diagram shows large deviations. The INT/Mix2 model reaches a surface nitrogen abundance that is about 0.4 dex higher than the baseline value.

Contrary to the first three cases, the SURF/Mix2 model has an extended blueward evolution, shown on the HRD and Kiel diagrams. Such a feature is commonly associated with blue stragglers, merger products, and quasi-chemically homogeneous evolution (e.g. Maeder 1987; Yoon et al. 2006; Knigge, Leigh & Sills 2009). Given the very efficient mixing in this model, it is nearly chemically homogeneous (c.f. Fig. 5). Indeed, the SURF/Mix2 model produces the highest nitrogen enrichment, more than 1 dex compared to the baseline in this configuration.

Even without considering magnetic braking, the two mixing schemes are considerably different, which leads to different evolutionary tracks. The assumptions regarding the mutual effect of the magnetic field and chemical mixing allow for a range of behaviours (see also Paper III). Models within the Mix1 scheme have modest differences as a result of using the different braking

[22]We use the spectroscopic definition of nitrogen abundance for the Hunter diagram, which is $\log(N/H) + 12$, where N and H are the surface number fraction of nitrogen and hydrogen. Note that mass fractions (which are the typical output quantities from evolutionary grids) need to be translated to number fraction by appropriate scaling.

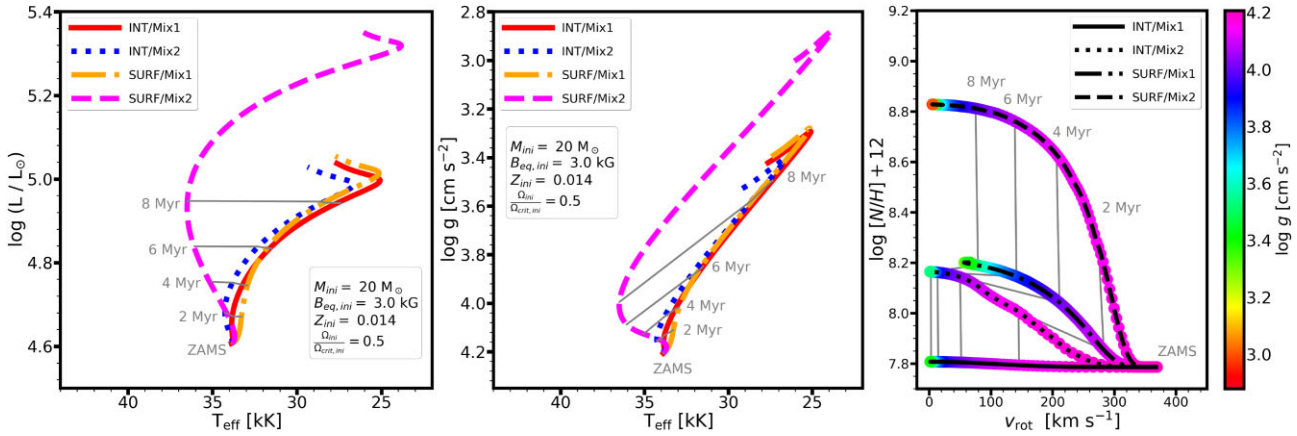

Figure 6. Fiducial evolutionary model with $M_{\rm ini} = 20\,{\rm M}_\odot$ at $Z = 0.014$ with $B_{\rm eq,\,ini} = 3$ kG within the INT/Mix1 scheme and the three other schemes, indicated with different colours and line-style. The grey lines connect equal ages. Panels from left to right show the HR, Kiel, and Hunter diagrams, respectively. The colour-coding shows the logarithmic surface gravity on the Hunter diagram.

schemes (INT/SURF). Models within the Mix2 scheme produce very efficient mixing, which is more easily quenched in the INT models than in the SURF models. The INT braking scheme, in contrast to the SURF, decreases the overall rotation rate, and the INT/Mix2 models do not evolve significantly blueward on the HRD. However, quasi-chemically homogeneous evolution is achieved in the case of non-magnetic Mix2 models, as well as in some magnetic SURF/Mix2 models depending on the initial field strength and stellar mass (see Figs E3 and E4, in the Appendix (Supplementary)). For example, the magnetic model in the SURF/Mix2 scheme leads to quasi-chemically homogeneous evolution for most of the main sequence (≈9 Myr out of 12 Myr) of a 20 M$_\odot$ model at solar metallicity with a 3 kG magnetic field. However, for the same initial field strength, the initially 60 M$_\odot$ model only experiences a brief phase of quasi-chemically homogeneous evolution and then evolves redwards (Fig. E4 (Supplementary)).

In summary, the braking and mixing schemes can drastically change the main observable characteristics. For example, the 8 Myr isochrone spans over a 10 kK effective temperature range (left-hand panel of Fig. 6) despite the models being initially completely identical. (When the 'extreme' case of SURF/Mix2, which is assumed to represent stars with complex magnetic fields and very efficient mixing, is not considered the difference is less, around 2 kK.) Thus the uncertainties associated with braking and mixing schemes in evolutionary model predictions are significant. From the Hunter diagram, we can conclude that various braking and mixing schemes can cover a wide range of rotation rates and surface nitrogen abundances. Three models already reach slow rotation (<50 km s^{-1}) with high surface gravities. Both INT models take less than 6 Myr to achieve this, while it is slightly over 8 Myr for the SURF/Mix2 model. The SURF/Mix1 model reaches the TAMS with a somewhat higher rotation rate than the other models.

3.2.2 *HRD evolution of a grid of magnetic models*

Fig. 7 shows the model predictions on the HRD colour-coded by the surface equatorial rotational velocity. Here the INT/Mix1 and INT/Mix2 schemes are displayed (see Figs E2 and E4 in the Appendix (Supplementary) for the SURF schemes) and we demonstrate the impact of a magnetic field with an initial equatorial field strength of 500 G.

In the INT models, strong magnetic braking leads to a rapid decrease of surface rotational velocity in the entire mass range from 3 to 60 M$_\odot$. This implies that rapidly rotating (single) magnetic massive stars are expected to be young and close to the ZAMS on the HRD. Some quantitative differences arise from the assumptions of the chemical mixing schemes. None the less, within the INT magnetic braking scheme these differences are small on the HRD, albeit it could affect the parameter determination (current age and mass) of known magnetic stars.

3.2.3 *Differential rotation on the Kiel diagram*

Fig. 8 shows the Kiel diagram. In the SURF models, radial differential rotation develops between the stellar core[23] and surface, as indicated with the grey contour lines. This is because we assume that a magnetic field with a complex geometry would only exert a strong torque on the near-surface layers by considering that organised, strong magnetic flux is not present in deeper stellar layers (see also Braithwaite & Nordlund 2006; Braithwaite 2008). Thus angular momentum transport in the deepest layers of the stellar envelope is dominated by – less efficient – hydrodynamical instabilities. On the other hand, in the INT models complete solid-body rotation is maintained throughout the main sequence. Similar to Fig. 6, where the 20 M$_\odot$ models are discussed, we see that the Mix1 and Mix2 chemical mixing schemes (within the SURF braking scheme here) result in notable differences in observable stellar parameters, which are the most prominent in the 5–10 M$_\odot$ range.

If the assumed magnetic field geometry remained unchanged throughout the main-sequence evolution, the prediction for magnetic massive stars is that differential rotation could be best identified in hotter, more massive, and more evolved (lower log g) stars. An important caveat nevertheless is the time evolution of complex magnetic fields. According to Braithwaite (2008), complex fields may simplify to a dipolar form since higher-order harmonics diffuse more rapidly. Indeed, Shultz et al. (2019b) finds that evolved magnetic stars tend to have simpler geometries (however, see also Kochukhov et al. 2019). Insofar it remains unclear what the exact diffusion time of complex magnetic flux tubes would be (perhaps still longer than the main-sequence lifetime) and whether the corresponding effects which

[23]Here, we use the MESA output quantity of core angular velocity '`center_omega`' to determine the rotation of the stellar core. The exact radius to obtain $\Omega_{\rm c}$ is not essential since the entire stellar core has the same angular velocity.

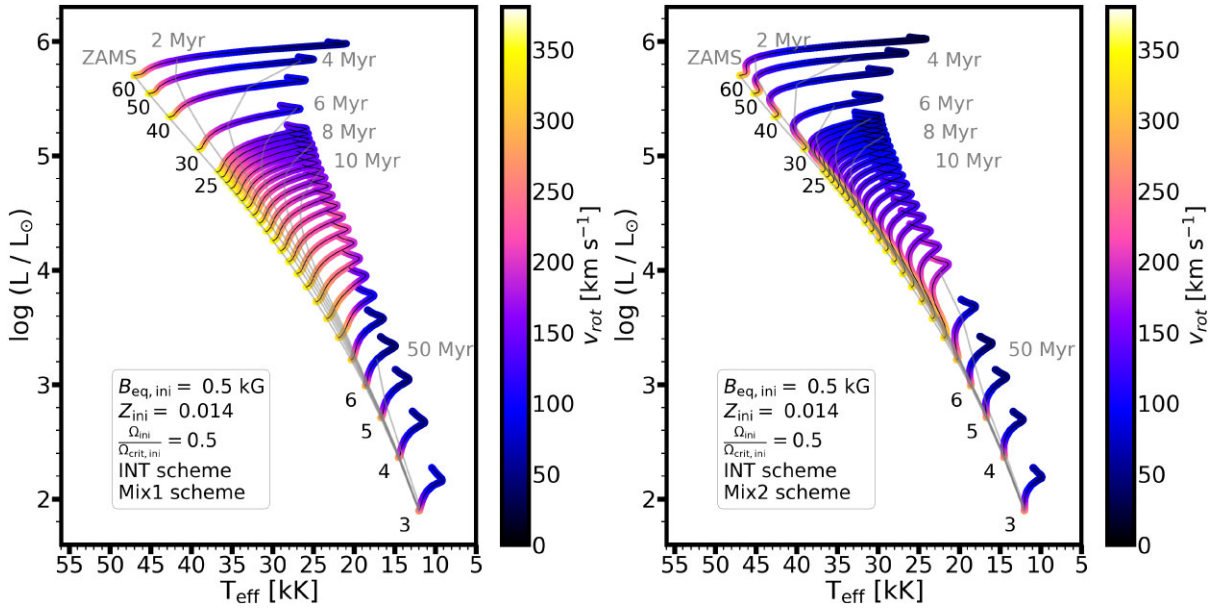

Figure 7. Hertzsprung–Russell diagram of magnetic single-star evolutionary models with initial magnetic field strength $B_{eq,\,ini} = 0.5$ kG, initial rotation rates of $\Omega_{ini}/\Omega_{ini,\,crit} = 0.5$ at solar $Z_{ini} = 0.014$ metallicity within the INT/Mix1 scheme (left-hand panel) and INT/Mix2 scheme (right-hand panel). The SURF schemes are shown in Figs E2 and E4 in the Appendix (Supplementary). Isochrones with grey lines indicate the time evolution from ZAMS to 50 Myr. The initial masses in solar units are given next to the ZAMS of the models (between 6 and 25 $M_\odot$, the increment is 1 $M_\odot$). The colour-bar shows how the equatorial rotational velocity evolves.

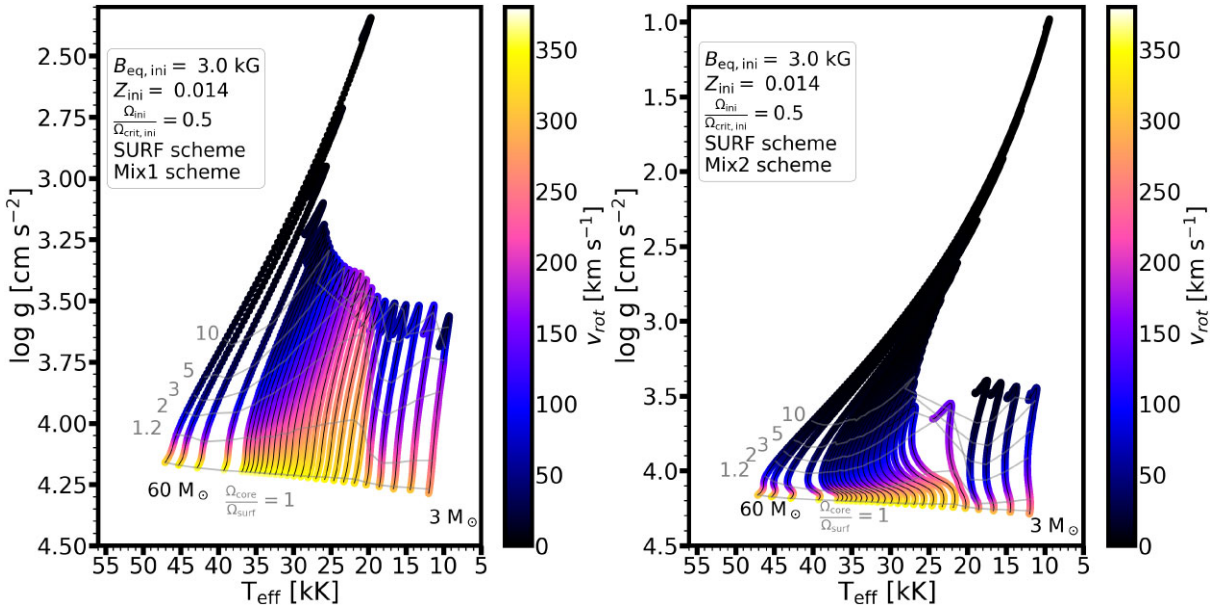

Figure 8. Kiel diagram of magnetic evolutionary models with $B_{eq,\,ini} = 3$ kG, $\Omega_{ini}/\Omega_{ini,\,crit} = 0.5$ at solar metallicity $Z_{ini} = 0.014$. within the SURF/Mix1 (left-hand panel) and SURF/Mix2 (right-hand panel) schemes. The grey contour lines indicate the unitless degree of differential rotation, quantified as the ratio of core to surface angular velocity. Note that Fig. 7 shows INT models where solid-body rotation ($\Omega_{core}/\Omega_{surf} = 1$) is achieved throughout the main sequence (see also Fig. D1 (Supplementary)). The initial masses of the models decrease from left to right. The colour-coding shows the surface equatorial rotational velocity.

are modelled in evolutionary codes (angular momentum transport, magnetic braking, mass-loss quenching) would change significantly. We evaluated the models with different initial field strengths and found that a stronger magnetic field is able to achieve a higher degree of differential rotation in comparison to models with lower field strengths. It would therefore be of great importance to obtain seismic data of a sample of magnetic massive stars.

3.2.4 Mass-dependent rotational evolution

Both the HRD and Kiel diagrams presented above[24] show the same distinctive feature. Namely, irrespective of how fast the spin-down per given scheme is, the mid-mass range models ($\approx$ 5–10 $M_\odot$, the

[24]See Figs E2–E4 in the Appendix (Supplementary) for the other schemes.

transition typically taking place at around 5–7 $M_\odot$ depending on model assumptions) always maintain a higher rotational velocity than models with other masses. This is the most striking on the left-hand panel of Fig. 8 for the SURF/Mix1 scheme. (The exact model behaviour was also recognised for a 5 and 10 $M_\odot$ model in Paper II .) The distinctive feature is a consequence of the spin-down of the models, which does not scale linearly with mass. For higher-mass models, wind mass loss contributes to the spin-down. The spin-down time to reach a given surface rotation takes a lower fractional age when the mass increases for initial masses higher than 10 $M_\odot$. Since stars below about 5 $M_\odot$ have much longer nuclear time-scales than higher-mass stars, even if magnetic braking is less efficient due to weaker winds, the available time-scale allows for braking the rotation at a lower fractional main-sequence age. This results in stars below 5 $M_\odot$ rotating more slowly at the TAMS than in the 5–10 $M_\odot$ range. We emphasise that the extent of the tracks on the HRD is not linear with stellar age: a significant time evolution can take place in a narrow location on the HRD close to the ZAMS as demonstrated by the isochrones. For example, the 50 $M_\odot$ model spends the first 2 Myr of its evolution while decreasing its $T_{\rm eff}$ by only about 5 kK, whereas in the second 2 Myr of its evolution, its $T_{\rm eff}$ decreases by about 15 kK (Fig. 7). Moreover, from 0 to 4 Myr, the 25 $M_\odot$ track evolves roughly 0.2 dex in luminosity and a few kK in $T_{\rm eff}$, which is a typical range of observational uncertainties depending on data quality and knowledge of distance and extinction. The precise age determination of young stars especially at initial masses below 25 $M_\odot$ becomes rather challenging with uncertainties well exceeding 1 Myr.

In summary, stars evolve slowly in the HRD at the beginning of the main sequence phase, and thus suffer strong magnetic braking while not evolving away from the ZAMS (in effective temperature and luminosity). However the interplay between the dependence on the initial mass of the meridional current velocity, the evolutionary time-scale near the ZAMS and the evolution of the radius produces a small bump of the surface rotational velocity in the initial mass range of 5–10 $M_\odot$ (see also Paper II). At the TAMS, this gives rise to a slower rotational velocity in models below 5 $M_\odot$ than models in the mid-mass range.

3.2.5 *Impact of varying the initial equatorial magnetic field strength*

Fig. 9 shows the impact of the initial equatorial magnetic field strength within the INT/Mix1 scheme on the HRD, Kiel, and Hunter diagrams for models from 3 to 60 $M_\odot$. The colour-coding of the surface rotational velocity on the HRD and Kiel diagrams show that for initial masses above 30 $M_\odot$, stellar winds play a significant role in depleting the angular momentum reservoir, and thus even without magnetic fields those stars can significantly spin-down on the main sequence. However, in the mass range from 3 to 30 $M_\odot$ single-star models would not undergo a dramatic angular momentum loss unless they were strongly magnetised. As demonstrated in the figure, the stronger the magnetic field, the more rapidly the surface rotation brakes. In particular, already a 3 kG equatorial field would produce a (sub)population of stars whose surface rotation is less than 50 km s^{-1} throughout essentially the entire main sequence.

The Kiel diagram shows yet another consequence of magnetic fields. Apart from the highest-mass models ($> 30 M_\odot$), the models with stronger magnetic fields tend to reach the end of the main sequence with higher surface gravities. For example, for a 10 $M_\odot$ model, the TAMS value of $\log g$ increases from 3.3 to 3.4 and to 3.5 from the 0 kG to the 0.5 kG and to the 3 kG models, respectively. Non-magnetic models maintain a higher rotation and thus the mixing remains more efficient. This mixing (if not too strong to keep the star in a bluer position in the HRD) tends to enlarge the convective core and consequently, extend the width of the main sequence towards lower effective temperatures and higher surface gravities.

The Hunter diagram reveals that the magnetic models may strongly deviate from non-magnetic model predictions. The stronger the magnetic field, the more rapidly rotation brakes, and the less nitrogen can be mixed to the stellar surface. We identify and demonstrate that there exists a cutoff magnetic field strength, above which no surface enrichment is expected given that it leads to a shorter magnetic braking time-scale compared to the rotational mixing time-scale. However, this cutoff field strength is strongly model and parameter dependent, and thus the exact value varies for given stellar mass, initial rotation, metallicity, and mixing scheme, amongst others. We evaluate this in Section 4.2.

3.2.6 *Impact of metallicity*

Fig. 10 shows the impact of the initial metallicity (here, for LMC and SMC values; the Solar metallicity models with the same input are shown in the lower panels of Fig. 9) for 3 to 60 $M_\odot$ models with initial equatorial magnetic field strengths of 3 kG within the INT/Mix1 scheme on the HRD, Kiel, and Hunter diagrams. At lower metallicity, the ZAMS is shifted to higher effective temperatures given that the stellar models are more compact due to the lower opacity and lower mean molecular weight. Specifically, the lower CNO abundances impose further contraction of a star to initiate core burning.

Magnetic braking, in our formalism, is metallicity independent. However, rotational mixing is not. The various mixing prescriptions depend on chemical composition and their gradients, which in turn affects the evolution of surface rotational velocity as most prominently revealed on the Kiel diagrams. For example, for a given value of a diffusion coefficient, the mixing time-scale is $\tau \approx R^2/D_{\rm chem}$. Since stars are more compact in lower Z, the time-scale becomes shorter. Consequently, the changes in rotation and surface abundances can be more impacted in lower metallicity stars.

Similarly, the highest relative nitrogen enrichment is seen when metallicity is the lowest (see also e.g. Brott et al. 2011a; Georgy et al. 2013). Let us recall that Fig. 10 shows the INT/Mix1 models, which – in our approach – are the lowest estimates for the surface enrichment (c.f. Fig. 6). The other schemes predict higher surface nitrogen enrichment when combining the effects with low metallicity. The trends produced in magnetic massive star models are unique since they lead to simultaneous surface nitrogen enrichment and a rapid spin-down of the stellar surface (c.f. Paper I , Paper II). The rapid spin-down could otherwise only be expected for very massive stars with extremely strong stellar winds.

4 DISCUSSION

4.1 Slowly-rotating, nitrogen-enriched stars in the LMC

The projected rotational velocities of massive stars in the Magellanic Clouds appear to follow a bi-modal distribution (e.g. Rivero González et al. 2012; Dufton et al. 2013, 2018, 2019, 2020; Ramírez-Agudelo et al. 2013, 2015). The bi-modality is also observed for intermediate-mass stars up to about 5 $M_\odot$ (e.g. Bastian et al. 2020; Sun et al. 2021). The observed slowly-rotating red main-sequence stars and rapidly-rotating blue main-sequence stars are thought to be evidence for main sequence splitting (e.g. Bastian et al. 2020) and an extended main sequence turn-off (e.g. D'Antona et al. 2015). It has been suggested

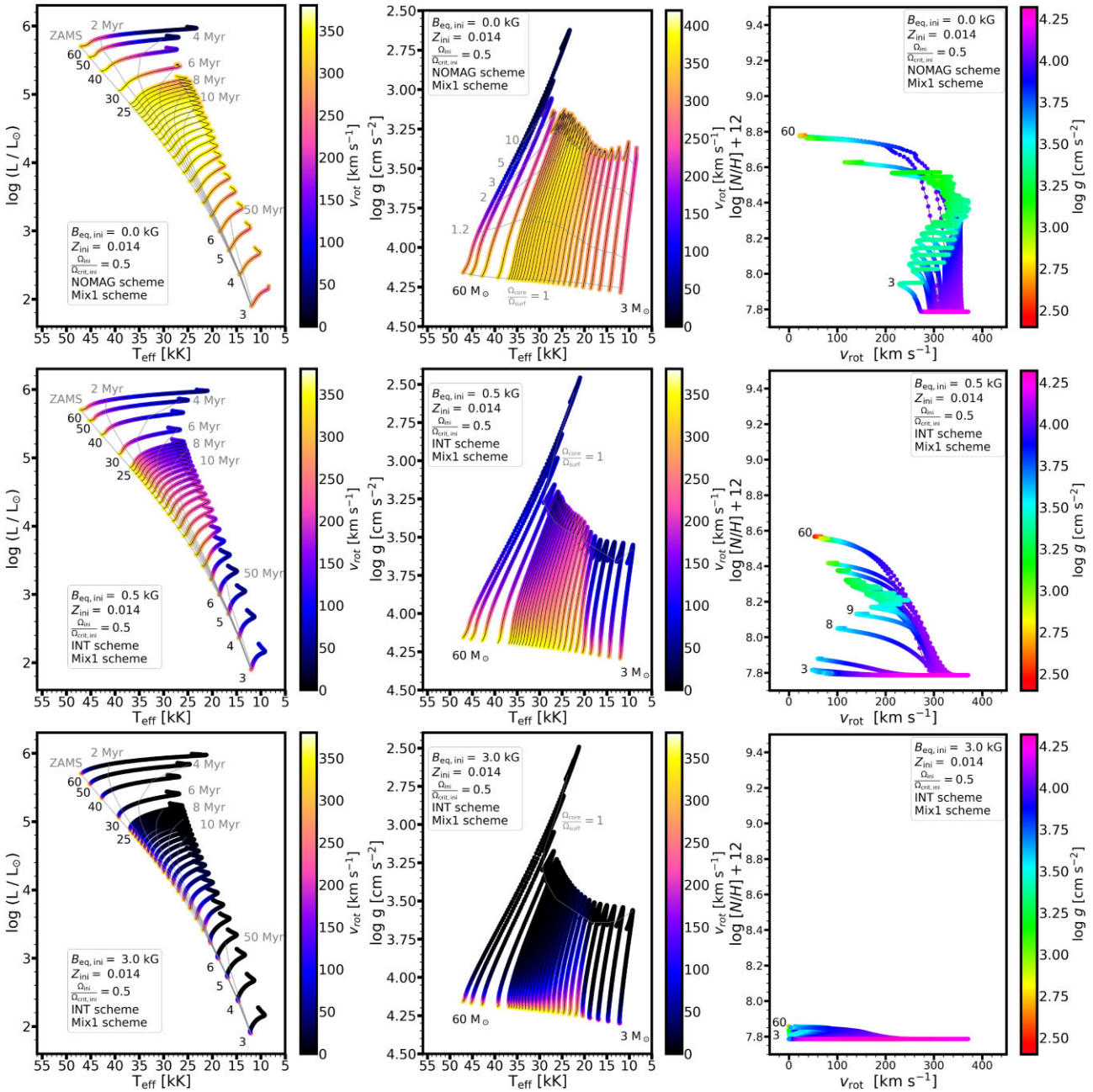

Figure 9. Evolutionary models from 3 to 60 $M_\odot$ at $Z = 0.014$ with varying the initial equatorial magnetic field strength (0, 0.5, 3 kG from top to bottom), within the INT/Mix1 magnetic braking and chemical mixing schemes. Panels from left to right show the HRD, Kiel, and Hunter diagrams. The colour-coding denotes surface rotational velocity on the first two panels, while it denotes the logarithmic surface gravity on the right-hand panel.

that the low-velocity peak might be caused by magnetic braking (e.g. Wolff, Edwards & Preston 1982; Sun et al. 2021). Shultz et al. (2018) demonstrated that the dichotomy in $v \sin i$ between Galactic B-type stars with and without magnetic fields is at least qualitatively consistent with the lower $v \sin i$ values observed in the magnetic population. For observed massive stars in the Magellanic Clouds, a notable fraction of slow-rotators were found to show measurable nitrogen enrichment, which challenges typical, non-magnetic single-star evolutionary models (Lennon et al. 1996; Lennon, Dufton & Crowley 2003; Dufton et al. 2006, 2013, 2018, 2019, 2020; Rivero González et al. 2012; Ramírez-Agudelo et al. 2013, 2015; McEvoy et al. 2015; Grin et al. 2017).

The nitrogen-enriched slow-rotators (also known as 'Group 2' stars, Hunter et al. 2008) correspond to roughly 20 per cent of the population in the LMC (e.g. Hunter et al. 2008; Brott et al. 2011b; Grin et al. 2017; Dufton et al. 2018). In the Galaxy, the observed incidence rate of fossil magnetism is found to be ≈ 10 per cent (e.g. Fossati et al. 2016; Grunhut et al. 2017; Sikora et al. 2019a) and it has previously been suggested that at least some of the Group 2 stars could be explained by magnetism (Meynet et al. 2011; Potter et al. 2012b, Paper I). This would require an incidence rate of fossil magnetism in the LMC that is likely higher than the 10 per cent observed in the Galaxy.[25] In addition, the (initial) magnetic field strength distribution is not yet known in our galaxy or in other

[25]For example, lower metallicity environments might favour a higher incidence rate of stars with fossil fields if the convective expulsion scenario, due

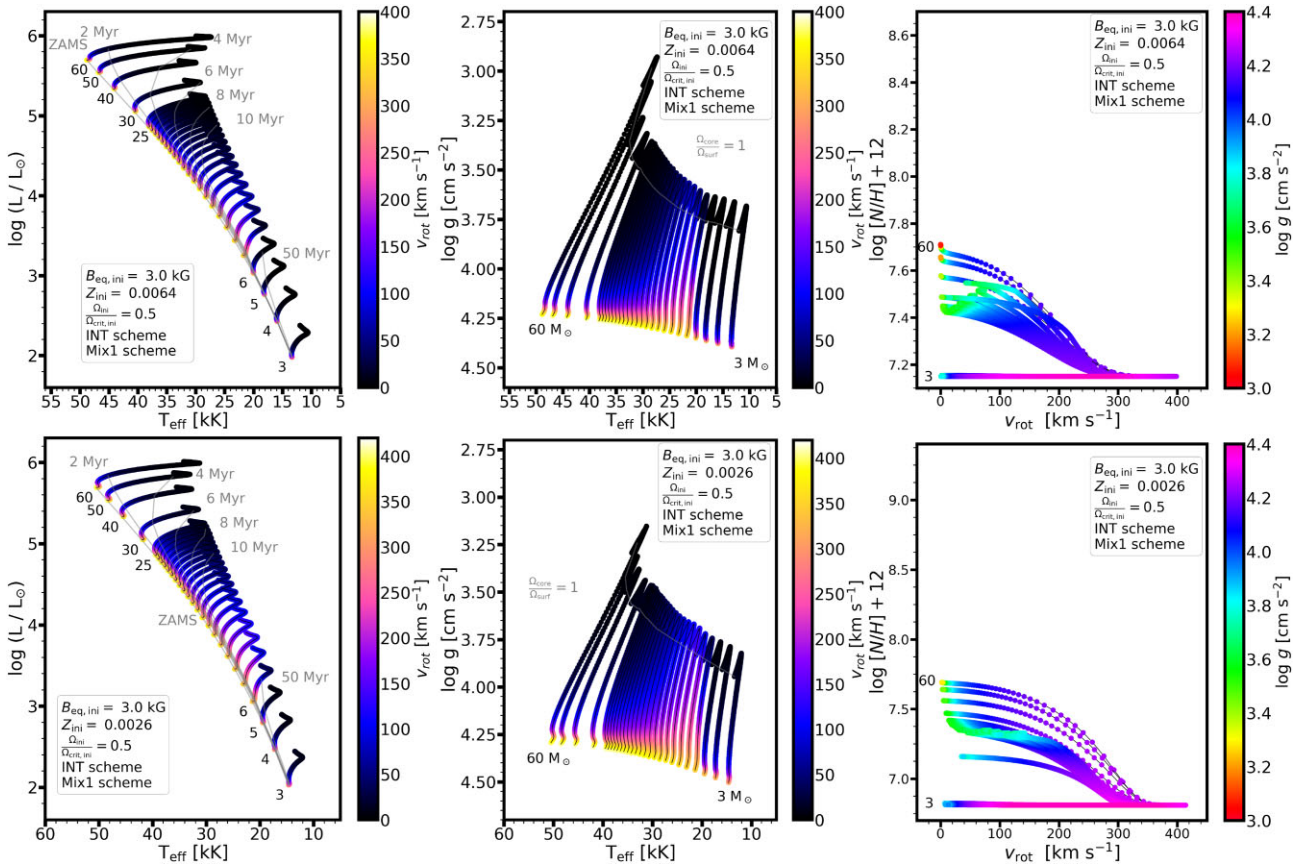

Figure 10. Same as Fig. 9 but varying the metallicity (upper – LMC, lower – SMC), within the INT/Mix1 scheme for an initial equatorial magnetic field strength of 3 kG.

metallicity environments; however, see Petit et al. (2019) and Cerrahoğlu et al. (2020) for theoretical models. It could also be that the Group 2 stars require an additional channel to explain all observations. In fact, binarity has been suggested by, e.g. Song et al. (2018b).

Fig. 11 shows the Hunter diagram with models representative of LMC metallicity ($Z = 0.0064$). Let us recall that we specifically adopted an initial nitrogen abundance in our models of $\log(N/H) + 12 = 7.15$ from Dopita et al. (2019) to produce evolutionary models guided by available empirical baseline abundance determinations. Here we demonstrate some of the complex parameter-space dependences that magnetic single-star models produce, albeit strongly depending on the model assumptions, especially the mixing and braking schemes (see also Meynet et al. 2011; Potter et al. 2012b, Paper I, Paper III). We display the non-magnetic models as well as magnetic models in the two braking and two mixing schemes. The initial equatorial magnetic field strength is 3 kG and the initial rotation is set by $\Omega_{ini}/\Omega_{ini,\,crit} = 0.5$. These assumptions produce evolutionary models, which over time reasonably approximate mean values measured from observations (magnetic field strengths from, e.g. Shultz et al. 2018 for Galactic magnetic B-type stars, and rotational velocities from, e.g. Dufton et al. 2013 for massive stars in the Magellanic Clouds). For example, the 3 kG initial ZAMS magnetic field strength weakens by roughly an order of magnitude (since $B_{eq} \propto R_\star^{-2}$ over time) at the TAMS to 300 G. Only models with initial masses from 15 to 60 $M_\odot$ are shown given that the available instrumentation allows magnitude limited observation of bright LMC stars that are more massive than $\approx 15\,M_\odot$ (e.g. Schneider et al. 2018). Thus the models are the most representative of O (and early B-type) stars.

Non-magnetic models (black and grey lines for the Mix1 and Mix2 schemes, respectively) mostly show high rotational velocities. Close to the TAMS, the NOMAG/Mix2 models spin-down efficiently and yield a high N/H ratio. However, this prediction is associated with producing Helium stars since these models experience Wolf–Rayet type mass loss due to their quasi-chemically homogeneous main sequence evolution (see Section D2). This helps the significant decrease of the surface hydrogen abundance, and hence the N/H ratio can further increase. Given the high effective temperatures that these models show close to the TMAS, we do not expect that the non-magnetic models should match the observations of typical Group 2 stars.

Chemical mixing remains challenging to constrain. The schemes that we assume in this work cover a large area on the Hunter diagram, which represents modelling uncertainties. In our models, for a given initial rotation and initial magnetic field strength, the INT/Mix1 and SURF/Mix2 models lead to the smallest and highest amount of nitrogen enrichment, respectively (see also Fig. 6). The INT/Mix2 and SURF/Mix1 models produce similar results, although the latter models cover a narrower domain. In this sense, the Mix1 and Mix2 schemes are limiting cases in terms of the produced nitrogen enrichment from our models. In nature, the situation might be much more complex since, for example, the study of slowly-pulsating B-type stars reveals a diverse range of mixing profiles (Pedersen et al. 2021). The variation of these profiles over time is not yet quantified.

to the subsurface iron opacity bump, regulates the incidence rate (Jermyn & Cantiello 2020).

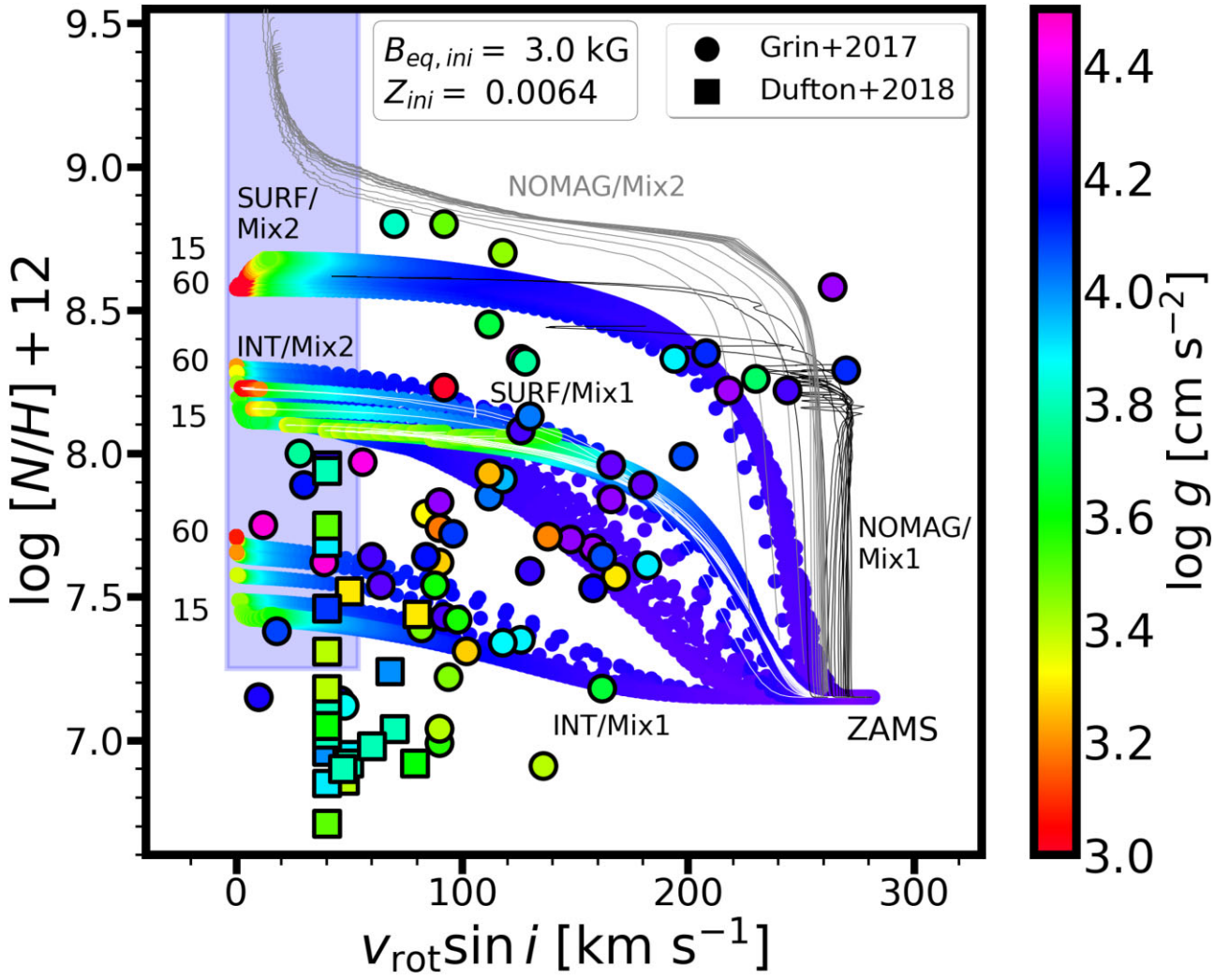

Figure 11. Hunter diagram of magnetic single-star evolutionary models with $B_{eq,\,ini} = 3$ kG, $\Omega_{ini}/\Omega_{ini,\,crit} = 0.5$ at LMC ($Z_{ini} = 0.0064$) metallicity within the four schemes. Models within the SURF/Mix1 scheme are also shown with white lines since they overlap with the INT/Mix2 models. Additionally, two sets of non-magnetic (NOMAG) models are shown within the Mix1 (grey) and Mix2 (black) schemes. For visualisation purposes, we reduced the numerical noise in the latter case. Models with initial masses from 15 to 60 $M_\odot$ are shown. The actual surface equatorial rotational velocity of the models is scaled by $\sin(\pi/4)$ to account for an average inclination angle. The coloured area corresponds to our definition of Group 2 stars. The colour-coding of the models shows the logarithmic surface gravity. Observations are shown with circles and squares, respectively. A typical reported uncertainty in the observed nitrogen abundances is about 0.1 dex.

The magnetic properties of stars in the LMC remain unknown. For this reason, the INT and SURF braking schemes represent assumptions and uncertainties that could only be resolved if, at least, upper limits on the magnetic field strengths were constrained. From the models we see that for a given initial magnetic field strength, the INT models produce less enrichment than the SURF models in a given mixing scheme.

In Fig. 11 we show abundance measurements[26] of observed massive stars at the LMC made by Grin et al. (2017) and Dufton et al. (2018). Since the observations only allow derivation of the projected rotational velocity $v \sin i$, we scale the actual rotational velocity in our models with $\sin(\pi/4)$ to account for an average inclination angle. We only consider here observations with $v \sin i < 300$ km s^{-1}.

[26]Although the observations of supergiants by McEvoy et al. (2015) are available, our models only cover the main sequence evolution and thus we refrain from a direct comparison to more evolved stars.

The observations reveal a large scatter, which likely represents a range of initial conditions (mass, rotation rates, magnetic field strength, binarity, etc.) and current age. The data from Grin et al. (2017) and Dufton et al. (2018) indicate stars in their main sequence evolutionary stages with surface gravities systematically decreasing towards lower rotation rates. Our models show that magnetic braking typically yields slowly-rotating stars early on in the evolution, still with high surface gravities. Once the rotation is slow (and $\log g$ is still ≈ 4.0), chemical mixing becomes inefficient and no further surface enrichment may be expected on the main sequence. This is the primary reason why magnetic models produce less surface enrichment than non-magnetic models with the same mixing assumptions (see also Fig. E1 (Supplementary)). However, at this point, the magnetic models still evolve further in time, albeit their location does not change in the Hunter diagram. Thus the magnetic models decrease their surface gravities (to $\log g \approx 3.0$) in a narrow region in the Hunter diagram, when their (assumed projected) surface rotational velocities are below 50 km s^{-2} in all cases, except for the

SURF/Mix1 models where the spin-down is the least efficient (c.f. Section 3.2.1).

There are several other caveats, which hamper a quantitative comparison between the models and observations. For example, the mass determinations are uncertain and often rely on (non-magnetic) evolutionary models. As we demonstrate in Fig. 11, even for an idealised situation where the braking and mixing schemes were known for a given magnetic field strength, the produced nitrogen enrichment is still a function of initial mass (see also Aerts et al. 2014; Maeder et al. 2014). In the INT/Mix1 scheme, the final nitrogen abundance becomes a factor of 2.5 higher when increasing the stellar mass from 15 to 60 $M_\odot$. This difference is less in the INT/Mix2 and SURF/Mix1 schemes (factor of ≈1.5), while this trend reverses for the SURF/Mix2 scheme.

Despite all these uncertainties, the models incorporating the effects of surface fossil magnetic fields can cover the region on the Hunter diagram where the 'anomalous' Group 2 stars (slow rotation along with surface nitrogen enrichment, see Hunter et al. 2008) are located, which is not possible with standard main sequence evolutionary models of single stars (see Martins et al. 2017 for non-magnetic $\approx$ 30 $M_\odot$ models in the Galaxy). In particular, for the slowly-rotating non-magnetic Mix2 models the produced nitrogen enrichment seems to be larger than indicated by observations, whereas the non-magnetic Mix1 models do not spin-down sufficiently.

Since the parameter space is degenerate, not only the mixing and braking scheme could produce results that cover Group 2 stars but also the variation of initial magnetic field strength in a given scheme. A stronger initial field would yield less enrichment (Fig. 9), possibly explaining the less nitrogen enriched stars, whereas a weaker initial field could be compatible with the most highly enriched stars (see Fig. E1 (Supplementary)). To quantify this, we introduce and discuss the cutoff magnetic field strength in the next section.

4.2 Cutoff magnetic field strengths in the LMC

It is of interest to evaluate a critical value of the magnetic field that strongly impacts observable properties. In particular, what range of initial magnetic field strengths allow for producing Group 2 stars? To this extent, we define a cutoff (maximum) field strength $B_{\rm max,\,N}$ as the initial equatorial magnetic field strength in a given model that allows for producing more than 0.1 dex of surface nitrogen enrichment (in spectroscopic units) during its main sequence evolution. If the initial magnetic field strength is higher than $B_{\rm max,\,N}$, then the mixing is inefficient due to the magnetic spin-down, and no nitrogen enrichment can be observed. Similar to the above definition, we may also define a cutoff (minimum) magnetic field strength that is the initial equatorial magnetic field strength needed to produce sufficiently slow rotators ($v_{\rm rot} < 71$ km s^{-1}) by the end of the main sequence evolution. Any value higher than $B_{\rm min,\,v}$ will yield slow-rotating models; however, values below $B_{\rm min,\,v}$ will still result in considerable rotational velocities at the TAMS. Fig. 12 shows the range of possible initial equatorial magnetic field strengths that are able to produce Group 2 stars given the constraints given above. $B_{\rm max,\,N}$ is shown with solid line and $B_{\rm min,\,v}$ with dashed line. The range is shown as a function of initial mass for the LMC (the Solar and SMC metallicity models are discussed in Appendix F (Supplementary)). The cutoff field strengths depend on the initial rotation rates, metallicity, mass, and chemical mixing and magnetic braking schemes. We discuss now the latter three.

Models within the INT/Mix1 scheme result in the lowest value of $B_{\rm max,\,N}$ since this scheme is the least efficient in chemical mixing. However, stronger magnetic fields would brake the rotation faster than the time-scale of rotational mixing. In contrast, models within the SURF/Mix2 scheme have such strong mixing that even a 50 kG equatorial field strength is insufficient to inhibit mixing.[27] A particular feature, a jump in $B_{\rm min,\,v}$ around 5 to 10 $M_\odot$, can be explained by the mass-dependent rotational behaviour of the models discussed in Section 3.2.4. In most models, the decreasing value of $B_{\rm min,\,v}$ for stars more massive than 10 $M_\odot$ implies that stronger stellar winds aid the spin-down thus a weaker magnetic field is sufficient to achieve slow-rotating stars.

We find that equatorial magnetic fields of initially a few kG are able to produce Group 2 stars in the INT/Mix1 scheme. Nevertheless, the range of allowed initial field strengths is the most limited in this case. In fact, models below 6 $M_\odot$ are in a 'forbidden' range where the minimum field strengths needed to brake rotation are higher than the maximum field strengths allowed to produce nitrogen enrichment. In the INT/Mix2 scheme, a much larger range of initial field strengths are allowed to produce Group 2 stars, particularly from 22 $M_\odot$, where the lower limit drops to 250 G. For initial masses higher than 7 $M_\odot$, the upper limit is of the order of 10 kG to produce Group 2 stars.

Models within the SURF/Mix1 and SURF/Mix2 schemes (right-hand panel of Fig. 12) cover a wide range of possible initial field strengths. The SURF/Mix1 scheme produces a similar mass-dependent pattern as the models in the INT scheme. Namely, models from 10 $M_\odot$ have systematically decreasing values of $B_{\rm min,\,v}$. However, for initial masses lower than 17 $M_\odot$ a 10 kG initial equatorial field strength is still needed to achieve slow rotation. Interestingly, for initial masses $\geq$ 19 $M_\odot$ there is a dip in $B_{\rm max,\,N}$, staying constant at 30 kG in contrast to the mass range of 7–18 $M_\odot$, where the 50 kG initial equatorial field strength still allows for producing nitrogen enrichment. The SURF/Mix2 models have a constant upper limit given by $B_{\rm max,\,N}$, meaning that even the strongest initial magnetic field strength we considered in this study is not sufficient to prevent nitrogen enrichment on the main sequence. The lower limit given by $B_{\rm min,\,v}$ is constant for initial masses higher than 6 $M_\odot$. In general, we can conclude that the INT scheme favours lower values for the cutoff magnetic field strengths of $B_{\rm max,\,N}$ to produce Group 2 stars and the SURF scheme allows for higher values of $B_{\rm max,\,N}$. It is quite remarkable that the upper limit remains roughly constant in the INT cases for stars more massive than about 10 $M_\odot$. In the SURF/Mix2 case, likely an unrealistically strong magnetic field would be needed to prevent nitrogen enrichment (as the 50 kG field is still insufficient). The Mix1 scheme tends to allow for a narrow range of values and Mix2 scheme covers a wide range of possible solutions.

In the LMC, both quantities used in our criteria, surface nitrogen abundance and (projected) rotational velocity, can be measured. Large-scale surveys dedicated to magnetic field measurements are not yet available in lack of high-resolution spectropolarimetry (however, see Bagnulo et al. 2017, 2020). This means that our predictions can be used as constraints on the strengths of magnetic fields that might exist in slowly-rotating, nitrogen-enriched ('Group 2') stars in the Magellanic Clouds. An initial equatorial magnetic field strength above $B_{\rm min,\,v}$ and below $B_{\rm max,\,N}$ will produce stars that can be identified as Group 2 stars.

[27] For visualisation purposes, we assigned 60 kG to those models where the maximum value in our grid of models (50 kG) was still insufficient to prevent nitrogen enrichment.

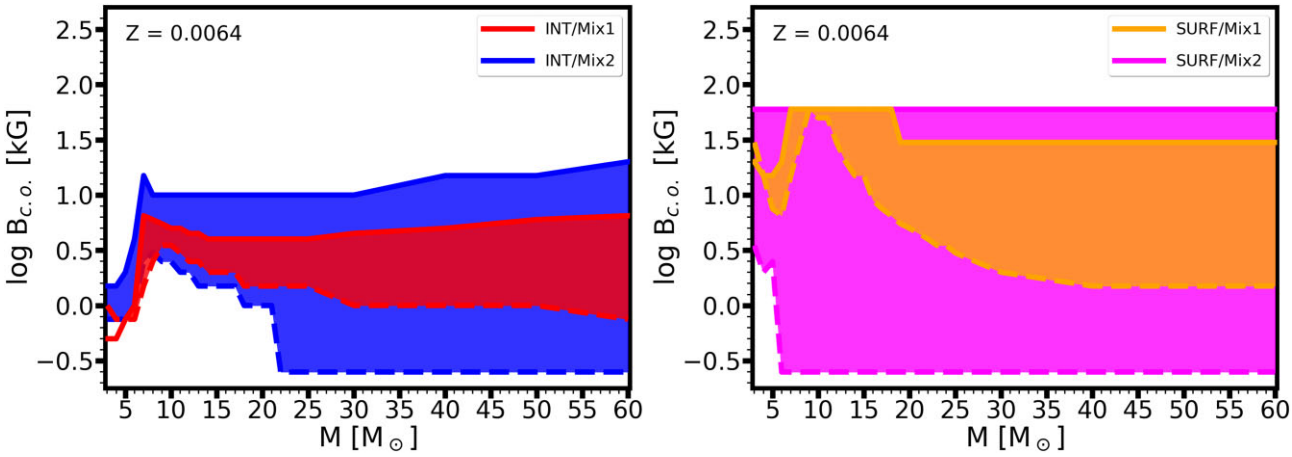

Figure 12. Cutoff magnetic field strengths as a function of mass to produce surface nitrogen enrichment ($B_{\mathrm{max,\,N}}$, solid line) and slow rotation ($B_{\mathrm{min,\,v}}$, dashed line). Values above $B_{\mathrm{max,\,N}}$ will inhibit surface nitrogen enrichment, whereas values below $B_{\mathrm{min,\,v}}$ will not spin-down the star sufficiently. Left/right-hand panels show the INT/SURF models. The models are considered for initially $\Omega/\Omega_{\mathrm{crit}} = 0.5$ at LMC ($Z = 0.0064$) metallicity.

4.3 Future work

The models presented in this work cover the main sequence phase of single stars. Logical extensions include calculating pre-main sequence models and continuing the computations to the post-main sequence phase to be able to scrutinise connections with end-products of stellar evolution, such as strongly magnetised white dwarfs and neutron stars (magnetars). The recently discovered link between magnetars and fast-radio bursts (Bochenek et al. 2020; CHIME/FRB Collaboration 2020) further supports investigations of the magnetic field origin of magnetars (e.g. Spruit 2009; Makarenko, Igoshev & Kholtygin 2021). Our grid of models could be further extended to cover initial masses below 3 $M_\odot$ and thus to compare with, for example, Ap stars. This requires some further considerations about the winds of these objects and the inclusion of atomic diffusion in the models. We assumed single-star models in this work. Some magnetic massive stars, such as τ Sco (Schneider et al. 2016, 2019, 2020; Keszthelyi et al. 2021), may challenge this scenario. None the less, the vast majority of OBA stars with fossil fields have characteristics that do not require invoking a merger event. In particular, fossil magnetic fields are detected in young massive stars, for example, in σ Ori E (Landstreet & Borra 1978; Townsend et al. 2010; Oksala et al. 2012; Song et al. 2022). Certain binary systems also present challenges to the merger scenario, such as the doubly-magnetic binary ϵ Lupi (Shultz et al. 2015) and the eclipsing late B-type binary HD 62658, which comprises two young nearly identical stars in a circularised orbit, only one of which is magnetic (Shultz et al. 2019c). Thus single-star models presented in this work are a reasonable first approach; however, future work remains to address binarity and mergers in combination with fossil field effects. In particular, multiplicity is common among massive stars (Sana et al. 2012, 2014; de Mink et al. 2013, 2014) and while close magnetic binary systems are rare (e.g. Alecian et al. 2013; Shultz et al. 2018), the mutual impact of magnetism and tidal interactions need to be further studied (e.g. Song et al. 2018a; Vidal et al. 2018).

The models computed in this work can be confronted with observations of known magnetic massive stars. They will complement previous approaches which relied on grids of stellar evolution models that did not include surface magnetic field effects (e.g. Brott et al. 2011a; Ekström et al. 2012; Chieffi & Limongi 2013; Choi et al. 2016) to infer stellar parameters and ages of magnetic stars. The differences are expected to be most pronounced for higher-mass stars (Petit et al. 2017), whereas – within the framework considered here – the lower-mass, A-type stars should be less impacted (Deal et al. 2021). None the less, the available *TESS* data and continuous spectropolarimetric monitoring can be used to constrain accurate rotation periods of such stars and directly compare with evolutionary models incorporating magnetic braking.

The INT models represent stars with strong, predominantly dipolar fields that are commonly identified in the sample of known magnetic massive stars. The SURF models are a limiting case motivated by stars with complex magnetic fields. In the future, the implementation of different magnetic field configurations and their time evolution could be considered to improve the present models.

The internal mixing efficiency remains uncertain in evolutionary modelling. In our models, quasi-chemically homogeneous evolution during the main sequence develops in the non-magnetic Mix2 case. In the INT/Mix2 models this behaviour is prevented by the efficient overall spin-down already when initially weak magnetic fields are considered, whereas in the SURF/Mix2 models a very efficient mixing still remains. The occurrence and duration of quasi-chemical evolution depends on the initial field strength and stellar mass; some SURF/Mix2 models evolve significantly bluewards, whereas some models turn to a redward evolution after mixing becomes less efficient (see Fig. D4 (Supplementary)). Quasi-chemically homogeneous evolution is expected to be rare in nature; however, it may be a crucial channel, for example, for some supernova events, gamma-ray bursts, or gravitational wave sources (e.g. Georgy et al. 2012; Martins et al. 2013; de Mink & Mandel 2016; Szécsi 2017).

Observational studies should help constrain the mixing efficiency and ultimately the physical mixing processes. As such, it would be beneficial to further study our models and confront them with measurements of surface nitrogen abundances in magnetic massive stars (Morel, Hubrig & Briquet 2008; Martins et al. 2012, 2015; Aerts et al. 2014; Morel et al. 2015), as well as studies which identified anomalous trends on the Hunter diagram in the LMC and SMC (e.g. Dufton et al. 2020, and see Section 4.1).

Finally, our current understanding of magnetic field evolution is still incomplete and, in particular, how different field geometries evolve over time is largely unconstrained. It will therefore be

valuable to explore various field evolution scenarios, for example, magnetic flux decay (Shultz et al. 2019b, Paper III). This might also lead to a time-dependent magnetic braking scheme depending on the relative dissipation time-scales of various complex field components.

5 CONCLUSIONS

In this work, we present the most extensive grid of stellar structure and evolution models taking into account the effects of surface fossil magnetic fields. The grid is publicly available on Zenodo and we recommend that, while acknowledging the uncertainties, it could be used to infer stellar parameters of known magnetic massive stars. No particular braking (INT/SURF) or mixing (Mix1/Mix2) scheme can be preferred at this time, although we do assume that if the field geometry is known, the INT case is applicable for dipolar fields and the SURF case for more complex geometries. Thus we consider the four schemes as limiting cases and, as we demonstrate in this work, the differences between these subgrids can substantially impact the determination of stellar parameters. It is therefore essential to confront the Mix1/Mix2 mixing schemes with spectroscopic studies even for stars where surface magnetic fields are not detected. In all cases (2 mixing schemes and 3 metallicities), we provide a subgrid of non-magnetic evolutionary models. Furthermore, the grid of models is suitable for population synthesis studies, which thus far have neglected magnetic field effects and magnetic massive stars within stellar populations (however, see Potter et al. 2012b). The impact of magnetic fields none the less may have important consequences on stellar populations and stellar-end products, for example, considering progenitors of magnetars (e.g. Schneider et al. 2019).

We demonstrate that magnetic braking by a fossil field leads to efficient spin-down. For example, an initial equatorial field of 3 kG strength at solar metallicity is sufficient in most models to decrease an initial surface equatorial rotational velocity of 300 km s^{-1} below 50 km s^{-1} within the early stages of the main sequence evolution (e.g. Fig. 8). For a given magnetic field strength, the spin-down of high-mass stars (>10 M$_\odot$) is further aided by mass loss, whereas the spin-down of lower-mass stars in our grid (<5 M$_\odot$) is identifiable due to the long nuclear time-scale. The intermediate-mass range (5–10 M$_\odot$) has the least efficient spin-down over the main sequence evolution.

The 'magnetic population' is thus far only identified within the Galaxy by spectropolarimetry and it is unknown what fraction of massive stars possesses strong, surface magnetic fields in extragalactic environments. Generally, the spin-down of the stellar surface for a given magnetic field strength is the most rapid at high metallicity (due to stronger winds), whereas the measurable surface nitrogen abundances are more impacted at lower metallicity (as chemical mixing effects are more pronounced). In the Large Magellanic Cloud, about 20 per cent of stars follow an anomalous pattern on the Hunter diagram, which can be covered with magnetic stellar evolution models. We identify the existence of a range of initial magnetic field strengths (the exact values depending on metallicity, mixing schemes, etc.) that allow for producing slowly-rotating, nitrogen-enriched Group 2 stars. The lower limit is constrained by a field strength that is needed to brake rotation and produce slow rotators. The upper limit is constrained by a field strength that is needed to allow for rotational mixing and still produce nitrogen enrichment. The range of possible field strengths for the INT models is much narrower than for the SURF models, however, it is compatible with typically measured values. In the LMC and SMC almost all (except some of the lowest mass) models lead to a solution. Contrary, we find that in the Galaxy the formation of Group 2 stars may essentially be prevented for initial masses from 6 to 23 M$_\odot$ in the INT/Mix1 scheme (Fig. E14 (Supplementary)).

Overall, we find significant differences between the braking and mixing schemes. With internal magnetic braking caused by a strong dipolar field, differential rotation cannot develop. With surface magnetic braking caused by a complex magnetic field the physical scenario remains much less clear; the results strongly depend on the chosen assumptions regarding chemical mixing.

ACKNOWLEDGEMENTS

We thank the anonymous referee for providing us with constructive comments. We thank the MESA developers for making their code publicly available. We also acknowledge the open-source code and detailed description of Fuller et al. (2019), which helped us with developing our implementation for the SURF models. Furthermore, we greatly appreciate discussions with Henk Spruit, Fabrice Martins, and Philip Dufton. Support for YG was provided by NASA through the NASA Hubble Fellowship Program grant #*HST*-HF2-51457.001-A awarded by the Space Telescope Science Institute, which is operated by the Association of Universities for Research in Astronomy, Inc., for NASA, under contract NAS5-26555. GM acknowledges support from the Swiss National Science Foundation (project number 200020-172505). GM and CG have received funding from the European Research Council (ERC) under the European Union's Horizon 2020 research and innovation program (Grant Agreement No. 833925). ADU is supported by NASA under award number 80GSFC21M0002. SG acknowledges support from a NOVA grant for the theory of massive star formation. RH acknowledges support from the World Premier International Research Centre Initiative (WPI Initiative), MEXT, Japan; the IReNA AccelNet Network of Networks, supported by the National Science Foundation under Grant No. OISE-1927130; the ChETEC COST Action (CA16117), supported by COST (European Cooperation in Science and Technology) and ChETEC-INFRA (grant No 101008324) supported by the European Union's Horizon 2020 research and innovation programme. VP is supported by the National Science Foundation under Grant No. AST-2108455. MES acknowledges support from the Annie Jump Cannon fellowship, endowed by the Mount Cuba Astronomical Observatory and supported by the University of Delaware. AuD acknowledges support by the National Aeronautics and Space Administration through Chandra Award Number TM1-22001B issued by the Chandra X-ray Center which is operated by the Smithsonian Astrophysical Observatory for and on behalf of NASA under contract NAS8-03060. This work was carried out on the Dutch national e-infrastructure with the support of SURF Cooperative.

DATA AVAILABILITY

A full reproduction package is available on Zenodo, in accordance with the Research Data Management Plan of the Anton Pannekoek Institute for Astronomy at the University of Amsterdam: https://doi.org/10.5281/zenodo.7069766.

The data used in this paper amounts to the order of 1/3 TB. A typical evolutionary model ('history' file in MESA nomenclature) is a few MBs, whereas a typical structure model ('profile' file in MESA nomenclature) is 10 MB. Each evolutionary model has three structure models saved at the ZAMS, mid-MS, and TAMS, respectively. In addition to the evolutionary and structure files, we save and provide the '.mod' files of each run when available. This allows for continuing the computations on the post-main sequence. We also generated

isochrones for each sub-grid, these are included in the Zenodo record.

Given the large range of covered parameter space, the output data in this paper is particularly useful for stellar evolution and population synthesis studies, as well as to compare with observational results of even individual stars. However, we emphasise that when interpreting observational results the modelling assumptions and uncertainties should be considered.

REFERENCES

Aerts C., Mathis S., Rogers T. M., 2019, ARA&A, 57, 35
Aerts C., Molenberghs G., Kenward M. G., Neiner C., 2014, ApJ, 781, 88
Aerts C., Puls J., Godart M., Dupret M. A., 2009, A&A, 508, 409
Aerts C., Thoul A., Daszyńska J., Scuflaire R., Waelkens C., Dupret M. A., Niemczura E., Noels A., 2003, Science, 300, 1926
Aguilera-Dena D. R., Langer N., Antoniadis J., Müller B., 2020, ApJ, 901, 114
Akgün T., Reisenegger A., Mastrano A., Marchant P., 2013, MNRAS, 433, 2445
Alecian E., Tkachenko A., Neiner C., Folsom C. P., Leroy B., 2016, A&A, 589, A47
Alecian E., Wade G. A., Catala C., 2009, in Strassmeier K. G., Kosovichev A. G., Beckman J. E., eds, Cosmic Magnetic Fields: From Planets, to Stars and Galaxies, Vol. 259. Cambridge Univ. Press, Cambridge, p. 445
Alecian E., Wade G. A., Catala C., Grunhut J. H., Landstreet J. D., Böhm T., Folsom C. P., Marsden S., 2013, MNRAS, 429, 1027
Alfvén H., 1942, Nature, 150, 405
Aloy M. Á., Obergaulinger M., 2021, MNRAS, 500, 4365
Angulo C. et al., 1999, Nucl. Phys. A, 656, 3
Asplund M., Grevesse N., Sauval A. J., 2005, in Barnes T. G., III, Bash F. N., eds, ASP Conf. Ser. Vol. 336, Cosmic Abundances as Records of Stellar Evolution and Nucleosynthesis. Astron. Soc. Pac., San Francisco, p. 25
Asplund M., Grevesse N., Sauval A. J., Scott P., 2009, ARA&A, 47, 481
Augustson K. C., Brun A. S., Toomre J., 2016, ApJ, 829, 92
Aurière M. et al., 2007, A&A, 475, 1053
Babel J., Montmerle T., 1997, A&A, 323, 121
Bagnulo S. et al., 2017, A&A, 601, A136
Bagnulo S. et al., 2020, A&A, 635, A163
Barker A. J., Jones C. A., Tobias S. M., 2019, MNRAS, 487, 1777
Barker A. J., Jones C. A., Tobias S. M., 2020, MNRAS, 495, 1468
Bastian N., Kamann S., Amard L., Charbonnel C., Haemmerlé L., Matt S. P., 2020, MNRAS, 495, 1978
Beloborodov A. M., 2009, ApJ, 703, 1044
Björklund R., Sundqvist J. O., Puls J., Najarro F., 2021, A&A, 648, A36
Bochenek C. D., Ravi V., Belov K. V., Hallinan G., Kocz J., Kulkarni S. R., McKenna D. L., 2020, Nature, 587, 59
Bonaca A. et al., 2012, ApJ, 755, L12
Bouret J. C., Lanz T., Hillier D. J., 2005, A&A, 438, 301
Bouret J. C., Martins F., Hillier D. J., Marcolino W. L. F., Rocha-Pinto H. J., Georgy C., Lanz T., Hubeny I., 2021, A&A, 647, A134
Bowman D. M., Burssens S., Simón-Díaz S., Edelmann P. V. F., Rogers T. M., Horst L., Röpke F. K., Aerts C., 2020, A&A, 640, A36
Braithwaite J., 2008, MNRAS, 386, 1947
Braithwaite J., 2012, MNRAS, 422, 619
Braithwaite J., Nordlund Å., 2006, A&A, 450, 1077
Braithwaite J., Spruit H. C., 2004, Nature, 431, 819
Braithwaite J., Spruit H. C., 2017, R. Soc. Open Sci., 4, 160271
Brands S. A. et al., 2022, A&A, 663, A36
Brinkman H. E., den Hartogh J. W., Doherty C. L., Pignatari M., Lugaro M., 2021, ApJ, 923, 47
Briquet M. et al., 2012, MNRAS, 427, 483
Brott I. et al., 2011a, A&A, 530, A115
Brott I. et al., 2011b, A&A, 530, A116
Burssens S. et al., 2020, A&A, 639, A81
Busse F. H., 1981, Geophys. Astrophys. Fluid Dyn., 17, 215
Busse F. H., 1982, ApJ, 259, 759
Buysschaert B., Aerts C., Bowman D. M., Johnston C., Van Reeth T., Pedersen M. G., Mathis S., Neiner C., 2018, A&A, 616, A148
Caiazzo I. et al., 2021, Nature, 595, 39
Caleo A., Balbus S. A., Tognelli E., 2016, MNRAS, 460, 338
Cantiello M. et al., 2009, A&A, 499, 279
Cantiello M., Braithwaite J., 2011, A&A, 534, A140
Canuto V. M., Goldman I., Mazzitelli I., 1996, ApJ, 473, 550
Canuto V. M., Mazzitelli I., 1992, ApJ, 389, 724
Cassisi S., Potekhin A. Y., Pietrinferni A., Catelan M., Salaris M., 2007, ApJ, 661, 1094
Castor J. I., Abbott D. C., Klein R. I., 1975, ApJ, 195, 157
Castro N., Fossati L., Langer N., Simón-Díaz S., Schneider F. R. N., Izzard R. G., 2014, A&A, 570, L13
Cerrahoğlu P., Petit V., Keszthelyi Z., David-Uraz A., 2020, in Wade G., Alecian E., Bohlender D., Sigut A., eds, Stellar Magnetism: A Workshop in Honour of the Career and Contributions of John D. Landstreet, Vol. 11. Polish Astron. Soc., Warsaw, p. 178
Chaboyer B., Zahn J.-P., 1992, A&A, 253, 173
Chang E., Garaud P., 2021, MNRAS, 506, 4914
Charbonneau P., MacGregor K. B., 2001, ApJ, 559, 1094
Charbonnel C., Zahn J. P., 2007, A&A, 476, L29
Chieffi A., Limongi M., 2013, ApJ, 764, 21
CHIME/FRB Collaboration, 2020, Nature, 587, 54
Choi J., Dotter A., Conroy C., Cantiello M., Paxton B., Johnson B. D., 2016, ApJ, 823, 102
Chugunov A. I., Dewitt H. E., Yakovlev D. G., 2007, Phys. Rev. D, 76, 025028
Cohen D. H., de Messières G. E., MacFarlane J. J., Miller N. A., Cassinelli J. P., Owocki S. P., Liedahl D. A., 2003, ApJ, 586, 495
Commerçon B., Hennebelle P., Henning T., 2011, ApJ, 742, L9
Costa G., Bressan A., Mapelli M., Marigo P., Iorio G., Spera M., 2021, MNRAS, 501, 4514
Costa G., Girardi L., Bressan A., Marigo P., Rodrigues T. S., Chen Y., Lanza A., Goudfrooij P., 2019, MNRAS, 485, 4641
Cowling T. G., 1945, MNRAS, 105, 166
Crowther P. A., Lennon D. J., Walborn N. R., 2006, A&A, 446, 279
Crutcher R. M., 2012, ARA&A, 50, 29
Cyburt R. H. et al., 2010, ApJS, 189, 240
D'Antona F., Di Criscienzo M., Decressin T., Milone A. P., Vesperini E., Ventura P., 2015, MNRAS, 453, 2637
Das B., Chandra P., Wade G. A., 2020, MNRAS, 499, 702
David-Uraz A. et al., 2019, MNRAS, 487, 304
David-Uraz A. et al., 2021b, MNRAS, 504, 4841
David-Uraz A., Petit V., Shultz M. E., Fullerton A. W., Erba C., Keszthelyi Z., Seadrow S., Wade G. A., 2021a, MNRAS, 501, 2677
de Almeida E. S. G., Marcolino W. L. F., Bouret J. C., Pereira C. B., 2019, A&A, 628, A36
de Mink S. E., Langer N., Izzard R. G., Sana H., de Koter A., 2013, ApJ, 764, 166
de Mink S. E., Mandel I., 2016, MNRAS, 460, 3545
de Mink S. E., Sana H., Langer N., Izzard R. G., Schneider F. R. N., 2014, ApJ, 782, 7
Deal M., Cunha M. S., Keszthelyi Z., Perraut K., Holdsworth D. L., 2021, A&A, 650, A125
Denissenkov P. A., Pinsonneault M., 2007, ApJ, 655, 1157
Denissenkov P. A., Pinsonneault M., MacGregor K. B., 2009, ApJ, 696, 1823
Donati J. F. et al., 2006, MNRAS, 370, 629
Donati J. F., Babel J., Harries T. J., Howarth I. D., Petit P., Semel M., 2002, MNRAS, 333, 55
Donati J.-F., Landstreet J. D., 2009, ARA&A, 47, 333
Dopita M. A., Seitenzahl I. R., Sutherland R. S., Nicholls D. C., Vogt F. P. A., Ghavamian P., Ruiter A. J., 2019, AJ, 157, 50
Driessen F. A., Sundqvist J. O., Kee N. D., 2019b, A&A, 631, A172
Driessen F. A., Sundqvist J. O., Wade G. A., 2019a, Proc. IAU Symp. 346, High-Mass X-ray Binaries: Illuminating the Passage from Massive Binaries to Merging Compact Objects. Cambridge Univ. Press, Cambridge, p. 45

Duez V., Mathis S., 2010, A&A, 517, A58
Duez V., Mathis S., Turck-Chièze S., 2010, MNRAS, 402, 271
Dufton P. L. et al., 2013, A&A, 550, A109
Dufton P. L. et al., 2018, A&A, 615, A101
Dufton P. L., Evans C. J., Hunter I., Lennon D. J., Schneider F. R. N., 2019, A&A, 626, A50
Dufton P. L., Evans C. J., Lennon D. J., Hunter I., 2020, A&A, 634, A6
Dufton P. L., Ryans R. S. I., Simón-Díaz S., Trundle C., Lennon D. J., 2006, A&A, 451, 603
Eddington A. S., 1925, The Observatory, 48, 73
Eggenberger P., Meynet G., Maeder A., Hirschi R., Charbonnel C., Talon S., Ekström S., 2008, Ap&SS, 316, 43
Ekström S. et al., 2012, A&A, 537, A146
Endal A. S., Sofia S., 1978, ApJ, 220, 279
Erba C. et al., 2021, MNRAS, 506, 5373
Espinosa Lara F., Rieutord M., 2011, A&A, 533, A43
Featherstone N. A., Browning M. K., Brun A. S., Toomre J., 2009, ApJ, 705, 1000
Feiden G. A., 2016, A&A, 593, A99
Feiden G. A., Chaboyer B., 2012, ApJ, 761, 30
Feiden G. A., Chaboyer B., 2013, ApJ, 779, 183
Feiden G. A., Chaboyer B., 2014, ApJ, 789, 53
Ferguson J. W., Alexander D. R., Allard F., Barman T., Bodnarik J. G., Hauschildt P. H., Heffner-Wong A., Tamanai A., 2005, ApJ, 623, 585
Ferrario L., Melatos A., Zrake J., 2015, Space Sci. Rev., 191, 77
Ferrario L., Pringle J. E., Tout C. A., Wickramasinghe D. T., 2009, MNRAS, 400, L71
Ferrario L., Wickramasinghe D., Kawka A., 2020, Adv. Space Res., 66, 1025
Ferraro V. C. A., 1937, MNRAS, 97, 458
Fossati L. et al., 2016, A&A, 592, A84
Fricke K., 1968, ZAp, 68, 317
Fuller G. M., Fowler W. A., Newman M. J., 1985, ApJ, 293, 1
Fuller J., Cantiello M., Stello D., Garcia R. A., Bildsten L., 2015, Science, 350, 423
Fuller J., Ma L., 2019, ApJ, 881, L1
Fuller J., Piro A. L., Jermyn A. S., 2019, MNRAS, 485, 3661
Fullerton A. W., Massa D. L., Prinja R. K., 2006, ApJ, 637, 1025
Gagnier D., Rieutord M., Charbonnel C., Putigny B., Espinosa Lara F., 2019a, A&A, 625, A88
Gagnier D., Rieutord M., Charbonnel C., Putigny B., Espinosa Lara F., 2019b, A&A, 625, A89
Georgy C. et al., 2013, A&A, 558, A103
Georgy C., Ekström S., Meynet G., Massey P., Levesque E. M., Hirschi R., Eggenberger P., Maeder A., 2012, A&A, 542, A29
Georgy C., Meynet G., Ekström S., Wade G. A., Petit V., Keszthelyi Z., Hirschi R., 2017, A&A, 599, L5
Giacomazzo B., Zrake J., Duffell P. C., MacFadyen A. I., Perna R., 2015, ApJ, 809, 39
Goldreich P., Schubert G., 1967, ApJ, 150, 571
Goldstein J., Townsend R. H. D., Zweibel E. G., 2019, ApJ, 881, 66
Gough D. O., Tayler R. J., 1966, MNRAS, 133, 85
Gräfener G., Owocki S. P., Vink J. S., 2012, A&A, 538, A40
Grasha K., Roy A., Sutherland R. S., Kewley L. J., 2021, ApJ, 908, 241
Gregory S. G., 2011, Am. J. Phys., 79, 461
Grin N. J. et al., 2017, A&A, 600, A82
Groh J. H. et al., 2019, A&A, 627, A24
Grunhut J. H. et al., 2012, MNRAS, 419, 1610
Grunhut J. H. et al., 2017, MNRAS, 465, 2432
Harrington P. Z., Garaud P., 2019, ApJ, 870, L5
Heger A., Langer N., Woosley S. E., 2000, ApJ, 528, 368
Heger A., Woosley S. E., Spruit H. C., 2005, ApJ, 626, 350
Hennebelle P., 2013, A&A, 556, A153
Henrichs H. F. et al., 2013, A&A, 555, A46
Henyey L., Vardya M. S., Bodenheimer P., 1965, ApJ, 142, 841
Høiland K., 1941, Avhandliger Norske Videnskaps-Akademi i Oslo, I,math.-naturv. Klasse, 11, 1
Holgado G., 2022, preprint (arXiv:2207.12776)
Howarth I. D., Siebert K. W., Hussain G. A. J., Prinja R. K., 1997, MNRAS, 284, 265
Huang W., Gies D. R., McSwain M. V., 2010, ApJ, 722, 605
Hunter I. et al., 2008, ApJ, 676, L29
Hunter I. et al., 2009, A&A, 496, 841
Iglesias C. A., Rogers F. J., 1993, ApJ, 412, 752
Iglesias C. A., Rogers F. J., 1996, ApJ, 464, 943
Irwin A. W., 2004, The FreeEOS Code for Calculating the Equation of State for Stellar Interiors. Available at: http://freeeos.sourceforge.net/
Itoh N., Hayashi H., Nishikawa A., Kohyama Y., 1996, ApJS, 102, 411
Jardine M., Barnes J. R., Donati J.-F., Collier Cameron A., 1999, MNRAS, 305, L35
Jermyn A. S., Cantiello M., 2020, ApJ, 900, 113
Jermyn A. S., Schwab J., Bauer E., Timmes F. X., Potekhin A. Y., 2021, ApJ, 913, 72
Keszthelyi Z. et al., 2020, MNRAS, 493, 518 (Paper II)
Keszthelyi Z., Meynet G., Georgy C., Wade G. A., Petit V., David-Uraz A., 2019, MNRAS, 485, 5843 (Paper I)
Keszthelyi Z., Meynet G., Martins F., de Koter A., David-Uraz A., 2021, MNRAS, 504, 2474 (Paper III)
Keszthelyi Z., Puls J., Wade G. A., 2017b, A&A, 598, A4
Keszthelyi Z., Wade G. A., Petit V., 2017a, in Eldridge J. J., Bray J. C., McClelland L. A. S., Xiao L., eds, Proc. IAU Symp. 329, The Lives and Death-Throes of Massive Stars. Cambridge Univ. Press, Cambridge, p. 250
Khalack V. R., Zverko J., Žižňovský J., 2003, A&A, 403, 179
Kippenhahn R., 1974, in Tayler R. J., Hesser J. E., eds, Proc. IAU Symp. 66, Late Stages of Stellar Evolution. D. Reidel Publishing Company, Dordrecht, p. 20
Kissin Y., Thompson C., 2018, ApJ, 862, 111
Knigge C., Leigh N., Sills A., 2009, Nature, 457, 288
Kochukhov O., Bagnulo S., 2006, A&A, 450, 763
Kochukhov O., Shultz M., Neiner C., 2019, A&A, 621, A47
Kochukhov O., Wade G. A., 2016, A&A, 586, A30
Körtgen B., Soler J. D., 2020, MNRAS, 499, 4785
Krtička J., 2014, A&A, 564, A70
Krtička J., Kubát J., 2017, A&A, 606, A31
Krtička J., Kubát J., Krtičková I., 2021, A&A, 647, A28
Kudritzki R.-P., Puls J., 2000, ARA&A, 38, 613
Kulsrud R. M., 2005, Plasma Physics for Astrophysics. Princeton Univ. Press, Princeton
Kuroda T., Arcones A., Takiwaki T., Kotake K., 2020, ApJ, 896, 102
Lamers H. J. G. L. M., Snow T. P., Lindholm D. M., 1995, ApJ, 455, 269
Landstreet J. D. et al., 2008, A&A, 481, 465
Landstreet J. D., 1991, in Tuominen I., Moss D., Rüdiger G., eds, The Boundary Between the Magnetic Fields of Ap-Stars and the Fields of Solar-Type Stars. Springer, Berlin, p. 342
Landstreet J. D., Bagnulo S., Andretta V., Fossati L., Mason E., Silaj J., Wade G. A., 2007, A&A, 470, 685
Landstreet J. D., Borra E. F., 1978, ApJ, 224, L5
Langanke K., Martínez-Pinedo G., 2000, Nucl. Phys. A, 673, 481
Laplace E., 2022, Astronomy and Computing, 38, 100516
Lavail A., Kochukhov O., Hussain G. A. J., Argiroffi C., Alecian E., Morin J., BinaMIcS Collaboration, 2020, MNRAS, 497, 632
Lecoanet D., Bowman D. M., Van Reeth T., 2022, MNRAS, 512, L16
Lennon D. J., Dufton P. L., Crowley C., 2003, A&A, 398, 455
Lennon D. J., Dufton P. L., Mazzali P. A., Pasian F., Marconi G., 1996, A&A, 314, 243
Leto P. et al., 2018, MNRAS, 476, 562
Leto P. et al., 2021, MNRAS, 507, 1979
Lodders K., 2003, ApJ, 591, 1220
Lovekin C. C., 2020, Front. Astron. Space Sci., 6, 77
Lucy L. B., Solomon P. M., 1970, ApJ, 159, 879
Lydon T. J., Sofia S., 1995, ApJS, 101, 357
MacDonald J., Mullan D. J., 2017, ApJ, 850, 58
MacDonald J., Petit V., 2019, MNRAS, 487, 3904

Mackey J., Lim A. J., 2011, MNRAS, 412, 2079
Maeder A., 1987, A&A, 178, 159
Maeder A., 1997, A&A, 321, 134
Maeder A., 2009, Physics, Formation and Evolution of Rotating Stars. Springer, Berlin
Maeder A., Meynet G., 2000, A&A, 361, 159
Maeder A., Meynet G., 2003, A&A, 411, 543
Maeder A., Meynet G., 2004, A&A, 422, 225
Maeder A., Meynet G., 2005, A&A, 440, 1041
Maeder A., Meynet G., Lagarde N., Charbonnel C., 2013, A&A, 553, A1
Maeder A., Przybilla N., Nieva M.-F., Georgy C., Meynet G., Ekström S., Eggenberger P., 2014, A&A, 565, A39
Maeder A., Zahn J.-P., 1998, A&A, 334, 1000
Makarenko E. I., Igoshev A. P., Kholtygin A. F., 2021, MNRAS, 504, 5813
Marcolino W. L. F. et al., 2012, MNRAS, 422, 2314
Markova N., Puls J., 2008, A&A, 478, 823
Markova N., Puls J., Langer N., 2018, A&A, 613, A12
Martayan C., Frémat Y., Hubert A. M., Floquet M., Zorec J., Neiner C., 2006, A&A, 452, 273
Martayan C., Frémat Y., Hubert A. M., Floquet M., Zorec J., Neiner C., 2007, A&A, 462, 683
Martin A. J. et al., 2018, MNRAS, 475, 1521
Martins F. et al., 2015, A&A, 575, A34
Martins F., Depagne E., Russeil D., Mahy L., 2013, A&A, 554, A23
Martins F., Escolano C., Wade G. A., Donati J. F., Bouret J. C., Mimes Collaboration, 2012, A&A, 538, A29
Martins F., Simón-Díaz S., Barbá R. H., Gamen R. C., Ekström S., 2017, A&A, 599, A30
Masada Y., Takiwaki T., Kotake K., 2022, ApJ, 924, 75
McEvoy C. M. et al., 2015, A&A, 575, A70
Mestel L., 1967, in Cameron R. C., ed., Magnetic and Related Stars. Springer, Berlin, p. 101
Mestel L., 1968, MNRAS, 138, 359
Mestel L., 1989, Quart. J. R. Astron. Soc., 30, 239
Mestel L., 1999, Stellar Magnetism. Oxford Univ. Press, Oxford
Mestel L., 2003, in Balona L. A., Henrichs H. F., Medupe R., eds, ASP Conf. Ser. Vol. 305, Magnetic Fields in O, B and A Stars: Origin and Connection to Pulsation, Rotation and Mass Loss. Astron. Soc. Pac., San Francisco, p. 3
Mestel L., Moss D., 2010, MNRAS, 405, 1845
Meynet G., Eggenberger P., Maeder A., 2011, A&A, 525, L11
Meynet G., Ekstrom S., Maeder A., Eggenberger P., Saio H., Chomienne V., Haemmerlé L., 2013, in Goupil M., Belkacem K., Neiner C., Lignières F., Green J. J., eds, Seismology for Studies of Stellar Rotation and Convection, Lecture Notes in Physics, Vol. 865, Lecture Notes in Physics. Springer Verlag, Berlin, p. 3
Michielsen M., Aerts C., Bowman D. M., 2021, A&A, 650, A175
Mokiem M. R. et al., 2007, A&A, 473, 603
Morel T. et al., 2015, in Meynet G., Georgy C., Groh J., Stee P., eds, Proc. IAU Symp. 307, New Windows on Massive Stars. Cambridge Univ. Press, Cambridge, p. 342
Morel T., Hubrig S., Briquet M., 2008, A&A, 481, 453
Moss D., 2003, A&A, 403, 693
Mösta P., Ott C. D., Radice D., Roberts L. F., Schnetter E., Haas R., 2015, Nature, 528, 376
Moyano F. D., Eggenberger P., Meynet G., Gehan C., Mosser B., Buldgen G., Salmon S. J. A. J., 2022, A&A, 663, A180
Muijres L. E., Vink J. S., de Koter A., Müller P. E., Langer N., 2012, A&A, 537, A37
Mullan D. J., MacDonald J., 2001, ApJ, 559, 353
Munoz M. S., Wade G. A., Nazé Y., Puls J., Bagnulo S., Szymański M. K., 2020, MNRAS, 492, 1199
Murphy L. J. et al., 2021, MNRAS, 501, 2745
Nazé Y., Petit V., Rinbrand M., Cohen D., Owocki S., ud-Doula A., Wade G. A., 2014, ApJS, 215, 10
Neiner C. et al., 2017, MNRAS, 471, 1926
Neiner C., Mathis S., Alecian E., Emeriau C., Grunhut J., BinaMIcS, MiMeS Collaborations, 2015, in Nagendra K. N., Bagnulo S., Centeno R., Jesús Martínez González M., eds, Proc. IAU Symp. 305, Polarimetry. Cambridge Univ. Press, Cambridge, p. 61
Neronov A., Vovk I., 2010, Science, 328, 73
Nieva M.-F., Przybilla N., 2012, A&A, 539, A143
Nugis T., Lamers H. J. G. L. M., 2002, A&A, 389, 162
Oda T., Hino M., Muto K., Takahara M., Sato K., 1994, At. Data Nucl. Data Tables, 56, 231
Oksala M. E., Grunhut J. H., Kraus M., Borges Fernandes M., Neiner C., Condori C. A. H., Campagnolo J. C. N., Souza T. B., 2015, A&A, 578, A112
Oksala M. E., Wade G. A., Marcolino W. L. F., Grunhut J., Bohlender D., Manset N., Townsend R. H. D., Mimes Collaboration, 2010, MNRAS, 405, L51
Oksala M. E., Wade G. A., Townsend R. H. D., Owocki S. P., Kochukhov O., Neiner C., Alecian E., Grunhut J., 2012, MNRAS, 419, 959
Owocki S. P., Shultz M. E., ud-Doula A., Sundqvist J. O., Townsend R. H. D., Cranmer S. R., 2020, MNRAS, 499, 5366
Owocki S. P., ud-Doula A., 2004, ApJ, 600, 1004
Owocki S. P., ud-Doula A., Sundqvist J. O., Petit V., Cohen D. H., Townsend R. H. D., 2016, MNRAS, 462, 3830
Park J., Prat V., Mathis S., Bugnet L., 2021, A&A, 646, A64
Parker E. N., 1958, ApJ, 128, 664
Parker E. N., 1963, Interplanetary Dynamical Processes. Interscience Publishers, New York
Pauldrach A., Puls J., Kudritzki R. P., 1986, A&A, 164, 86
Paxton B. et al., 2013, ApJS, 208, 4
Paxton B. et al., 2015, ApJS, 220, 15
Paxton B. et al., 2018, ApJS, 234, 34
Paxton B. et al., 2019, ApJS, 243, 10
Paxton B., Bildsten L., Dotter A., Herwig F., Lesaffre P., Timmes F., 2011, ApJS, 192, 3
Pedersen M. G. et al., 2021, Nat. Astron., 5, 715
Petermann I., Langer N., Castro N., Fossati L., 2015, A&A, 584, A54
Petit V. et al., 2013, MNRAS, 429, 398
Petit V. et al., 2017, MNRAS, 466, 1052
Petit V. et al., 2019, MNRAS, 489, 5669
Petrov B., Vink J. S., Gräfener G., 2016, MNRAS, 458, 1999
Pinsonneault M. H., Kawaler S. D., Sofia S., Demarque P., 1989, ApJ, 338, 424
Poniatowski L. G. et al., 2021, A&A, 647, A151
Potekhin A. Y., Chabrier G., 2010, Contrib. Plasma Phys., 50, 82
Potter A. T., Chitre S. M., Tout C. A., 2012b, MNRAS, 424, 2358
Potter A. T., Tout C. A., Eldridge J. J., 2012a, MNRAS, 419, 748
Poutanen J., 2017, ApJ, 835, 119
Prat V., Guilet J., Viallet M., Müller E., 2016, A&A, 592, A59
Prinja R. K., Barlow M. J., Howarth I. D., 1990, ApJ, 361, 607
Prinja R. K., Massa D. L., 1998, in Howarth I., ed., ASP Conf. Ser. Vol. 131, Properties of Hot Luminous Stars. Astron. Soc. Pac., San Francisco, p. 218
Przybilla N., Nieva M. F., Irrgang A., Butler K., 2013, in Alecian G., Lebreton Y., Richard O., Vauclair G., eds, New Advances in Stellar Physics: From Microscopic to Macroscopic Processes, EAS Publications Series Vol. 63. p. 13
Przybilla N., Nieva M.-F., Butler K., 2008, ApJ, 688, L103
Puls J., Springmann U., Lennon M., 2000, A&AS, 141, 23
Puls J., Vink J. S., Najarro F., 2008, A&AR, 16, 209
Quentin L. G., Tout C. A., 2018, MNRAS, 477, 2298
Ramachandran V., Oskinova L. M., Hamann W. R., 2021, A&A, 646, A16
Ramírez-Agudelo O. H. et al., 2013, A&A, 560, A29
Ramírez-Agudelo O. H. et al., 2015, A&A, 580, A92
Reboul-Salze A., Guilet J., Raynaud R., Bugli M., 2021, A&A, 645, A109
Reese D. R., Mirouh G. M., Espinosa Lara F., Rieutord M., Putigny B., 2021, A&A, 645, A46
Reisenegger A., 2009, A&A, 499, 557
Rieutord M., 2006, in Rieutord M., Dubrulle B., eds, Stellar Fluid Dynamics and Numerical Simulations: From the Sun to Neutron Stars, EAS Publications Series Vol. 21. EDP Sciences, Les Ulis, France, p. 275
Rivero González J. G., Puls J., Najarro F., Brott I., 2012, A&A, 537, A79

Rivinius T., Townsend R. H. D., Kochukhov O., Štefl S., Baade D., Barrera L., Szeifert T., 2013, MNRAS, 429, 177
Rogers F. J., Nayfonov A., 2002, ApJ, 576, 1064
Rubio-Díez M. M., Sundqvist J. O., Najarro F., Traficante A., Puls J., Calzoletti L., Figer D., 2022, A&A, 658, A61
Salaris M., Cassisi S., 2017, R. Soc. Open Sci., 4, 170192
Sana H. et al., 2012, Science, 337, 444
Sana H. et al., 2014, ApJS, 215, 15
Saumon D., Chabrier G., van Horn H. M., 1995, ApJS, 99, 713
Schaller G., Schaerer D., Meynet G., Maeder A., 1992, A&AS, 96, 269
Schneider F. R. N. et al., 2018, A&A, 618, A73
Schneider F. R. N., Ohlmann S. T., Podsiadlowski P., Röpke F. K., Balbus S. A., Pakmor R., 2020, MNRAS, 495, 2796
Schneider F. R. N., Ohlmann S. T., Podsiadlowski P., Röpke F. K., Balbus S. A., Pakmor R., Springel V., 2019, Nature, 574, 211
Schneider F. R. N., Podsiadlowski P., Langer N., Castro N., Fossati L., 2016, MNRAS, 457, 2355
Schüssler M., Knölker M., 2001, in Mathys G., Solanki S. K., Wickramasinghe D. T., eds, ASP Conf. Ser. Vol. 248, Magnetic Fields Across the Hertzsprung-Russell Diagram. Astron. Soc. Pac., San Francisco, p. 115
Seifried D., Walch S., Weis M., Reissl S., Soler J., Klessen R., Joshi P., 2020, MNRAS, 497, 4196
Shultz M. E. et al., 2018, MNRAS, 475, 5144
Shultz M. E. et al., 2019b, MNRAS, 490, 274
Shultz M. E. et al., 2019c, MNRAS, 490, 4154
Shultz M. E. et al., 2020, MNRAS, 499, 5379
Shultz M. E., Kochukhov O., Labadie-Bartz J., David-Uraz A., Owocki S. P., 2021b, MNRAS, 507, 1283
Shultz M. E., Rivinius T., Wade G. A., Kochukhov O., Alecian E., David-Uraz A., Sikora J., 2021a, MNRAS, 504, 4850
Shultz M. E., Wade G. A., Rivinius T., Alecian E., Neiner C., Petit V., Wisniewski J. P., 2019a, MNRAS, 485, 1508
Shultz M., Wade G. A., Alecian E., BinaMIcS Collaboration, 2015, MNRAS, 454, L1
Sikora J. et al., 2019b, MNRAS, 487, 4695
Sikora J., Wade G. A., Power J., Neiner C., 2019a, MNRAS, 483, 3127
Simon-Diaz S., Godart M., Castro N., Herrero A., Aerts C., Puls J., Telting J., Grassitelli L., 2016, VizieR Online Data Catalog, pp J/A + A/597/A22
Simón-Díaz S., Godart M., Castro N., Herrero A., Aerts C., Puls J., Telting J., Grassitelli L., 2017, A&A, 597, A22
Simón-Díaz S., Herrero A., 2014, A&A, 562, A135
Solberg H., 1936, Astrophys. Nor., 1, 237
Song H. F. et al., 2018a, A&A, 609, A3
Song H. F. et al., 2022, A&A, 657, 60
Song H., Wang J., Song F., Zhang R., Li Z., Peng W., Zhan Q., Jing J., 2018b, ApJ, 859, 43
Spitzer L. J., 1958, in Lehnert B., ed., Proc. IAU Symp. 6, Electromagnetic Phenomena in Cosmical Physics. Cambridge Univ. Press, Cambridge, p. 169
Spruit H. C., 1979, Sol. Phys., 61, 363
Spruit H. C., 1999, A&A, 349, 189
Spruit H. C., 2002, A&A, 381, 923
Spruit H. C., 2004, in Maeder A., Eenens P., eds, Proc. IAU Symp. 215, Stellar Rotation. Astron. Soc. Pacific, San Francisco, p. 356
Spruit H. C., 2009, in Strassmeier K. G., Kosovichev A. G., Beckman J. E., eds, Proc. IAU Symp. 259, Cosmic Magnetic Fields: From Planets, to Stars and Galaxies. Cambridge Univ. Press, Cambridge, p. 61
Stello D., Cantiello M., Fuller J., Huber D., García R. A., Bedding T. R., Bildsten L., Silva Aguirre V., 2016, Nature, 529, 364
Stępień K., 2000, A&A, 353, 227
Sun W., Duan X.-W., Deng L., de Grijs R., 2021, ApJ, 921, 145
Sundqvist J. O., Björklund R., Puls J., Najarro F., 2019, A&A, 632, A126
Sundqvist J. O., Petit V., Owocki S. P., Wade G. A., Puls J., MiMeS Collaboration, 2013, MNRAS, 433, 2497
Sundqvist J. O., ud-Doula A., Owocki S. P., Townsend R. H. D., Howarth I. D., Wade G. A., 2012, MNRAS, 423, L21
Sweet P. A., 1950, MNRAS, 110, 548
Szécsi D., 2017, Contrib. Astron. Obs. Skalnate Pleso, 47, 108
Takahashi K., Langer N., 2021, A&A, 646, A19
Takiwaki T., Kotake K., 2011, ApJ, 743, 30
Takiwaki T., Kotake K., Sato K., 2009, ApJ, 691, 1360
Tao L., Weiss N. O., Brownjohn D. P., Proctor M. R. E., 1998, ApJ, 496, L39
Tayler R. J., 1973, MNRAS, 161, 365
Timmes F. X., Swesty F. D., 2000, ApJS, 126, 501
Tout C. A., Wickramasinghe D. T., Liebert J., Ferrario L., Pringle J. E., 2008, MNRAS, 387, 897
Townsend R. H. D. et al., 2013, ApJ, 769, 33
Townsend R. H. D., Oksala M. E., Cohen D. H., Owocki S. P., ud-Doula A., 2010, ApJ, 714, L318
Townsend R. H. D., Owocki S. P., 2005, MNRAS, 357, 251
Townsend R., 2020, MESA SDK for Linux. Available at: https://doi.org/10.5281/zenodo.4587206
Triana S. A., Moravveji E., Pápics P. I., Aerts C., Kawaler S. D., Christensen-Dalsgaard J., 2015, ApJ, 810, 16
Trundle C., Lennon D. J., 2005, A&A, 434, 677
Trundle C., Lennon D. J., Puls J., Dufton P. L., 2004, A&A, 417, 217
ud-Doula A., 2020, in Wade G., Alecian E., Bohlender D., Sigut A., eds, Stellar Magnetism: A Workshop in Honour of the Career and Contributions of John D. Landstreet, Vol. 11. Polish Astron. Soc., Warsaw, p. 140
ud-Doula A., Owocki S. P., 2002, ApJ, 576, 413
ud-Doula A., Owocki S. P., Townsend R. H. D., 2008, MNRAS, 385, 97
ud-Doula A., Owocki S. P., Townsend R. H. D., 2009, MNRAS, 392, 1022
ud-Doula A., Sundqvist J. O., Owocki S. P., Petit V., Townsend R. H. D., 2013, MNRAS, 428, 2723
ud-Doula A., Townsend R. H. D., Owocki S. P., 2006, ApJ, 640, L191
van Loon J. T., Cioni M. R. L., Zijlstra A. A., Loup C., 2005, A&A, 438, 273
Vidal J., Cébron D., Schaeffer N., Hollerbach R., 2018, MNRAS, 475, 4579
Villebrun F. et al., 2019, A&A, 622, A72
Vink J. S., Brott I., Gräfener G., Langer N., de Koter A., Lennon D. J., 2010, A&A, 512, L7
Vink J. S., de Koter A., Lamers H. J. G. L. M., 1999, A&A, 350, 181
Vink J. S., de Koter A., Lamers H. J. G. L. M., 2000, A&A, 362, 295
Vink J. S., de Koter A., Lamers H. J. G. L. M., 2001, A&A, 369, 574
Vink J. S., Sander A. A. C., 2021, MNRAS, 504, 2051
Vogt H., 1925, Astron. Nachr., 223, 229
Wade G. A. et al., 2016, MNRAS, 456, 2
Walborn N. R. et al., 2015, AJ, 150, 99
Walborn N. R., 1972, AJ, 77, 312
Weber E. J., Davis L., Jr., 1967, ApJ, 148, 217
Weiss N. O., 1966, Proc. R. Soc. A, 293, 310
Wickramasinghe D. T., Ferrario L., 2005, MNRAS, 356, 1576
Wickramasinghe D. T., Tout C. A., Ferrario L., 2014, MNRAS, 437, 675
Wolff S. C., Edwards S., Preston G. W., 1982, ApJ, 252, 322
Wright G. A. E., 1969, MNRAS, 146, 197
Wright G. A. E., 1973, MNRAS, 162, 339
Yıldız M., Yakut K., Bakış H., Noels A., 2006, MNRAS, 368, 1941
Yoon S. C., Langer N., Norman C., 2006, A&A, 460, 199
Zahn J. P., Brun A. S., Mathis S., 2007, A&A, 474, 145
Zahn J.-P., 1992, A&A, 265, 115

SUPPORTING INFORMATION

Supplementary data are available at *MNRAS* online.

IV_Grid_v_mnras_removed.pdf

Please note: Oxford University Press is not responsible for the content or functionality of any supporting materials supplied by the authors. Any queries (other than missing material) should be directed to the corresponding author for the article.

This paper has been typeset from a TEX/LATEX file prepared by the author.